

A stable partitioned FSI algorithm for rigid bodies and incompressible flow. Part II: General formulation

J. W. Banks^{a,2,4}, W. D. Henshaw^{a,2,3,*}, D. W. Schwendeman^{a,2,3}, Qi Tang^{a,1}

^a*Department of Mathematical Sciences, Rensselaer Polytechnic Institute, Troy, NY 12180, USA.*

Abstract

A stable partitioned algorithm is developed for fluid-structure interaction (FSI) problems involving viscous incompressible flow and rigid bodies. This *added-mass partitioned* (AMP) algorithm remains stable, without sub-iterations, for light and even zero mass rigid bodies when added-mass and viscous added-damping effects are large. The scheme is based on a generalized Robin interface condition for the fluid pressure that includes terms involving the linear acceleration and angular acceleration of the rigid body. Added mass effects are handled in the Robin condition by inclusion of a boundary integral term that depends on the pressure. Added-damping effects due to the viscous shear forces on the body are treated by inclusion of added-damping tensors that are derived through a linearization of the integrals defining the force and torque. Added-damping effects may be important at low Reynolds number, or, for example, in the case of a rotating cylinder or rotating sphere when the rotational moments of inertia are small. In this second part of a two-part series, the general formulation of the AMP scheme is presented including the form of the AMP interface conditions and added-damping tensors for general geometries. A fully second-order accurate implementation of the AMP scheme is developed in two dimensions based on a fractional-step method for the incompressible Navier-Stokes equations using finite difference methods and overlapping grids to handle the moving geometry. The numerical scheme is verified on a number of difficult benchmark problems.

Keywords: fluid-structure interaction; moving overlapping grids; incompressible Navier-Stokes; partitioned schemes; added-mass; added-damping; rigid bodies

*Department of Mathematical Sciences, Rensselaer Polytechnic Institute, 110 8th Street, Troy, NY 12180, USA.

Email addresses: banksj3@rpi.edu (J. W. Banks), henshw@rpi.edu (W. D. Henshaw), schwed@rpi.edu (D. W. Schwendeman), tangq3@rpi.edu (Qi Tang)

¹Research supported by the Eliza Ricketts Postdoctoral Fellowship.

²This work was supported by contracts from the U.S. Department of Energy ASCR Applied Math Program.

³Research supported by the National Science Foundation under grant DMS-1519934.

⁴Research supported by a U.S. Presidential Early Career Award for Scientists and Engineers.

Contents

| | | |
|-------------------|---|-----------|
| 1 | Introduction | 3 |
| 2 | Governing equations | 4 |
| 3 | Added-damping tensors | 6 |
| 4 | The added-mass and added-damping interface conditions | 8 |
| 5 | The AMP-RB time-stepping algorithm | 9 |
| 6 | Discrete and approximate added-damping tensors | 11 |
| 7 | Numerical approach using moving composite grids | 13 |
| 8 | Numerical Results | 15 |
| 8.1 | One-dimensional motion of a piston and a rectangular fluid chamber | 15 |
| 8.2 | Rotating disk in an annular fluid chamber | 18 |
| 8.3 | Zero mass disk in a counter-flow | 19 |
| 8.4 | Solid disk falling to the bottom of a fluid chamber | 23 |
| 8.5 | Rectangular body rising to the top of fluid chamber | 25 |
| 8.6 | Interaction between rising and falling bodies in a fluid chamber | 28 |
| 9 | Conclusions | 30 |
| Appendix A | Shear stress of an incompressible fluid on the surface of a rigid body | 32 |
| Appendix B | Example added-damping tensors for bodies of different shapes | 33 |
| Appendix B.1 | Cylinder and disk | 34 |
| Appendix B.2 | Rectangle | 34 |
| Appendix B.3 | Trapezoid | 35 |
| Appendix B.4 | L-shaped domain | 35 |
| Appendix B.5 | Ellipse | 36 |
| Appendix B.6 | Sphere | 36 |

1. Introduction

We describe a new numerical approach for fluid-structure interaction (FSI) problems involving the motion of rigid bodies in an incompressible fluid. The approach, referred to as the AMP-RB scheme, is a partitioned algorithm in which the equations for the fluid and the rigid bodies are handled using separate solvers. This is in contrast to monolithic schemes where the whole system of equations are solved simultaneously at each time step. A significant challenge for partitioned schemes is stability, especially for light bodies (or even zero-mass bodies) when the effects of added mass and added damping are important.⁵ In addition, it can be difficult to achieve second-order accuracy, or higher, for partitioned time-stepping schemes due to errors caused by the numerical treatment of the matching conditions at the interface between the fluid and the rigid bodies.

The AMP-RB scheme is based on a fractional-step approach for the fluid in which the velocity is advanced in one stage, and the pressure is determined in a second stage [1, 2]. The viscous terms in the stress tensor are handled implicitly so that the velocity can be advanced with a larger stable time step. The key ingredients of the AMP-RB scheme are contained in the added-mass partitioned (AMP) interface conditions which couple the equations of motion of the rigid body to a compatibility boundary condition for the pressure on the surface of the body. These conditions are derived at a continuous level by matching the *acceleration* of the body to that of the fluid. As a result, the integration of the equations of motion of the rigid-body are coupled strongly to the update of the fluid pressure; this ensures the proper balances of forces at the interface thereby suppressing instabilities due to added-mass effects. Suppressing instabilities due to added-damping is more subtle. The fluid forces on the body depend on the viscous shear stresses which, in turn, implicitly depend on the velocity of the body. This implicit dependence of the fluid forces on the body velocity is explicitly exposed and, after some simplifying approximations, is expressed in terms of *added-damping tensors* which are incorporated into the AMP interface conditions as a means to overcome added-damping instabilities.

This paper is the second of a two-part series of papers in which the AMP-RB scheme is developed and analyzed. The work in Part I [3] introduced the scheme and applied it to various model problems. A stability analysis of the AMP-RB scheme was performed, and it was shown that the new scheme remains stable, without sub-time-step iterations, even for light or zero-mass rigid bodies when added-mass and added-damping effects are large. In this paper, we extend the formulation of Part I to general three-dimensional configurations⁶. An important new feature in this extension is the generalization of the added-damping tensors that are incorporated into the AMP-RB scheme to treat the effects of added damping. Exact formulas are derived for the added-damping tensors which involve solutions to variational problems given by two discrete vector Helmholtz equations. Approximate added-damping tensors, convenient for use in AMP-RB scheme, are obtained using the results from the model problem analysis in Part I. These approximate tensors are readily evaluated at the initial time using surface integrals over a given body, which can be computed either analytically or numerically. The scheme is implemented in two dimensions for arbitrary body motions using moving overlapping grids [4, 5]. Numerical examples in two dimensions are provided that verify the accuracy and stability of the scheme for some challenging problems involving light and zero-mass rigid bodies.

The FSI regime involving incompressible flows and moving rigid bodies is of great practical and scientific interest. The reader is referred to the introduction of Part I for a discussion of the literature, particularly as related to the issue of added-mass instabilities for partitioned schemes. Here we note the long history of using composite overlapping (overset, Chimera) grids for simulating rigid bodies in fluids, going back to the early work on aircraft store-separation by Dougherty and Kuan [6]. Recent use of overlapping grids for simulating aircraft, rotorcraft, wind-turbines, rockets, spacecraft, ships and underwater vehicles can be found at the overset grid symposium website [7].

The remainder of the paper is organized as follows. The governing equations are given in Section 2. The analytic forms of the added-damping tensors are introduced in Section 3 and these are subsequently used in Section 4 to define the AMP-RB interface conditions. The AMP-RB time-stepping algorithm, which uses a fractional-step scheme for the velocity-pressure form of the Navier-Stokes equations is outlined in Section 5.

⁵A brief physical explanation of added-mass and added-damping effects is given in the Introduction of Part I.

⁶Even though the numerical results are restricted to two dimensions, we believe that the derivation and description of the added-damping tensors is more clearly presented in three dimensions.

Approximations to the added-damping tensors are developed in Section 6. Section 7 gives a brief outline of the moving overlapping grid approach. Numerical results are given in Section 8 and concluding remarks are made in Section 9. Appendix A provides the derivation of a formula for the shear stress used in determining the added-damping tensors, while Appendix B provides the explicit form of the added-damping tensors for some different shaped rigid bodies (e.g., rectangle, disk, sphere)

2. Governing equations

We consider the fluid-structure coupling of an incompressible fluid and one or more rigid bodies as illustrated in Figure 1, although the subsequent discussion will consider a single rigid body for simplicity. The fluid occupies the domain $\mathbf{x} \in \Omega(t)$ while the rigid body lies in the domain $\mathbf{x} \in \Omega_b(t)$, where \mathbf{x} is position and t is time. The coupling of the fluid and body occurs along the interface $\Gamma_b(t) = \bar{\Omega}(t) \cap \bar{\Omega}_b(t)$. It is assumed that the fluid is governed by the incompressible Navier-Stokes equations, which in an Eulerian frame are given by

$$\frac{\partial \mathbf{v}}{\partial t} + (\mathbf{v} \cdot \nabla) \mathbf{v} = \frac{1}{\rho} \nabla \cdot \boldsymbol{\sigma}, \quad \mathbf{x} \in \Omega(t), \quad (1)$$

$$\nabla \cdot \mathbf{v} = 0, \quad \mathbf{x} \in \Omega(t), \quad (2)$$

where ρ is the (constant) fluid density and $\mathbf{v} = \mathbf{v}(\mathbf{x}, t)$ is the fluid velocity. The fluid stress tensor, $\boldsymbol{\sigma} = \boldsymbol{\sigma}(\mathbf{x}, t)$, is given by

$$\boldsymbol{\sigma} = -p\mathbf{I} + \boldsymbol{\tau}, \quad \boldsymbol{\tau} = \mu [\nabla \mathbf{v} + (\nabla \mathbf{v})^T], \quad (3)$$

where $p = p(\mathbf{x}, t)$ is the pressure, \mathbf{I} is the identity tensor, $\boldsymbol{\tau}$ is the viscous stress tensor, and μ is the (constant) fluid viscosity. For future reference, the components of a vector such as \mathbf{v} will be denoted by v_m , $m = 1, 2, 3$ (i.e. $\mathbf{v} = [v_1, v_2, v_3]^T$), while components of a tensor such as $\boldsymbol{\sigma}$ will be denoted by σ_{mn} , $m, n = 1, 2, 3$. The velocity-divergence form of the equations given by (1) and (2) require appropriate initial and boundary conditions, as well as conditions on $\Gamma_b(t)$ where the behaviour of the fluid is coupled to that of the solid (as discussed below).

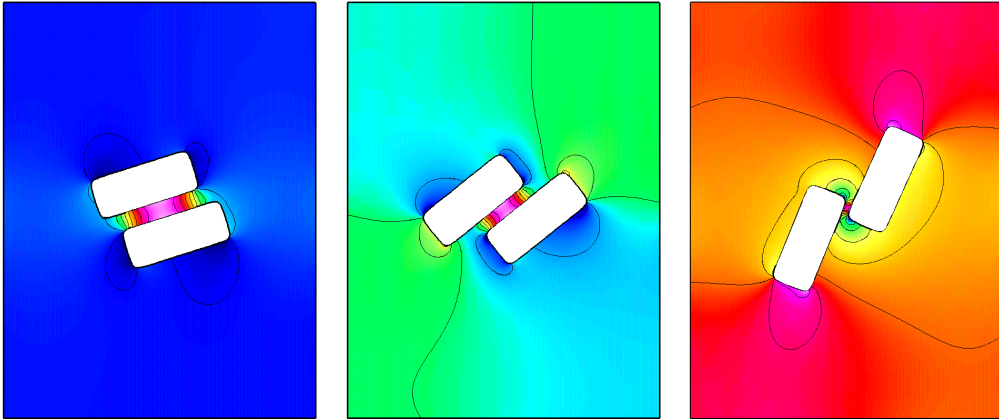


Figure 1: Two rectangular bodies moving through an incompressible fluid under the influence of gravity showing contours of the fluid pressure. Time increases from left to right. The heavier upper-body moves downward while the lighter lower-body rises.

An elliptic equation for the fluid pressure can be derived from (1)–(3) as

$$\Delta p = -\rho \nabla \mathbf{v} : (\nabla \mathbf{v})^T, \quad \mathbf{x} \in \Omega(t), \quad (4)$$

where

$$\nabla \mathbf{v} : (\nabla \mathbf{v})^T \stackrel{\text{def}}{=} \sum_{i=1}^3 \sum_{j=1}^3 \frac{\partial v_i}{\partial x_j} \frac{\partial v_j}{\partial x_i}.$$

In the velocity-pressure form of the incompressible Navier-Stokes equations, the Poisson equation (4) is used in place of (2). This form requires an additional boundary condition, and a natural choice is $\nabla \cdot \mathbf{v} = 0$ for $\mathbf{x} \in \partial\Omega(t)$, see [1] for example.

The rigid body is defined in terms of the translation and rotation of the centre of mass. In discussing the rigid body motion we use the following notation:

| | |
|---|--|
| $m_b \in \mathbb{R}$ | : mass of the rigid body, |
| $\rho_b \in \mathbb{R}$ | : density of the rigid body, |
| $\mathbf{I}_b(t) \in \mathbb{R}^{3 \times 3}$ | : moment of inertia matrix, |
| $\mathbf{x}_b(t) \in \mathbb{R}^3$ | : position of the centre of mass, |
| $\mathbf{v}_b(t) \in \mathbb{R}^3$ | : velocity of the centre of mass, |
| $\boldsymbol{\omega}_b(t) \in \mathbb{R}^3$ | : angular velocity, |
| $E_b(t) \in \mathbb{R}^{3 \times 3}$ | : matrix with columns being the principle axes of inertia, |
| $\mathbf{a}_b(t) \in \mathbb{R}^3$ | : linear acceleration of the centre of mass, |
| $\mathbf{b}_b(t) \in \mathbb{R}^3$ | : angular acceleration of the centre of mass, |
| $\mathbf{f}_e(t) \in \mathbb{R}^3$ | : external body force (e.g. gravity), |
| $\mathbf{g}_e(t) \in \mathbb{R}^3$ | : external torque. |

The equations of motion for the rigid body are then given by the Newton-Euler equations,

$$m_b \mathbf{a}_b = \int_{\Gamma_b} (-p \mathbf{n} + \boldsymbol{\tau} \mathbf{n}) dS + \mathbf{f}_e, \quad (5)$$

$$\mathbf{I}_b \mathbf{b}_b = -\boldsymbol{\omega}_b \times \mathbf{I}_b \boldsymbol{\omega}_b + \int_{\Gamma_b} (\mathbf{r} - \mathbf{x}_b) \times (-p \mathbf{n} + \boldsymbol{\tau} \mathbf{n}) dS + \mathbf{g}_e, \quad (6)$$

$$\dot{\mathbf{v}}_b = \mathbf{a}_b, \quad (7)$$

$$\dot{\mathbf{x}}_b = \mathbf{v}_b, \quad (8)$$

$$\dot{\boldsymbol{\omega}}_b = \mathbf{b}_b, \quad (9)$$

$$\dot{E}_b = \boldsymbol{\omega}_b \times E_b, \quad (10)$$

where \mathbf{r} denotes a point on the surface of the body and $\mathbf{n} = \mathbf{n}(\mathbf{r}, t)$ is the outward unit normal to the body. These equations of motion require initial conditions for $\mathbf{x}_b(0)$, $\mathbf{v}_b(0)$, $\boldsymbol{\omega}_b(0)$, and $E_b(0)$.

The motion of a point $\mathbf{r}(t)$ on the surface of the body is given by a translation together with a rotation about the initial centre of mass,

$$\mathbf{r}(t) = \mathbf{x}_b(t) + R(t)(\mathbf{r}(0) - \mathbf{x}_b(0)), \quad (11)$$

where $R(t)$ is the rotation matrix given by

$$R(t) = E_b(t) E_b^T(0). \quad (12)$$

The velocity and acceleration of that point are then given by

$$\dot{\mathbf{r}}(t) = \mathbf{v}_b(t) + \boldsymbol{\omega}_b \times (\mathbf{r}(t) - \mathbf{x}_b(t)), \quad \mathbf{r} \in \Gamma_b, \quad (13)$$

$$\ddot{\mathbf{r}}(t) = \mathbf{a}_b + \mathbf{b}_b \times (\mathbf{r} - \mathbf{x}_b) + \boldsymbol{\omega}_b \times [\boldsymbol{\omega}_b \times (\mathbf{r}(t) - \mathbf{x}_b(t))], \quad \mathbf{r} \in \Gamma_b. \quad (14)$$

On the interface between the fluid and solid, the fluid velocity must match the solid velocity. If $\mathbf{r} = \mathbf{r}(t)$ denotes a point on the surface of the body Γ_b , then the fluid velocity $\mathbf{v}(\mathbf{r}(t), t)$ at the surface satisfies

$$\mathbf{v}(\mathbf{r}(t), t) = \dot{\mathbf{r}}(t), \quad \mathbf{r} \in \Gamma_b, \quad (15)$$

where $\dot{\mathbf{r}}(t)$ is given in (13).

3. Added-damping tensors

Viscous shear stress on the surface of the rigid body generates forces and torques that are coupled to the motion of the rigid body. If this coupling is not properly treated, then a numerical scheme may become unstable due to an added-damping instability. Such an instability arises, for example, when an over-estimate of the shear stress leads to an over-correction of the rigid-body velocity, which in turn leads to an even larger over-estimate of the stress, and so on. In this section, we introduce exact formulas for the added-damping tensors that account for the coupling of the force and torque due to viscous shear stress and the motion of the rigid body. These tensors are then used in the description of the AMP-RB interface conditions given next in Section 4. For the numerical implementation of the AMP-RB interface conditions, we only require approximations of added-damping tensors, and these approximations are discussed in Section 6.

Added-damping effects, which arise from the forces and torques on the body due the viscous shear stress, are represented by the terms involving $\boldsymbol{\tau}\mathbf{n}$ in the surface integrals (5) and (6) for the linear and angular accelerations of the rigid body, respectively. These two contributions to the accelerations of the body are given by

$$\mathcal{F}_\mu(\mathbf{v}, \mathbf{v}_b, \boldsymbol{\omega}_b) = \int_{\Gamma_b} \boldsymbol{\tau}\mathbf{n} dS, \quad \mathcal{G}_\mu(\mathbf{v}, \mathbf{v}_b, \boldsymbol{\omega}_b) = \int_{\Gamma_b} (\mathbf{r} - \mathbf{x}_b) \times (\boldsymbol{\tau}\mathbf{n}) dS, \quad (16)$$

where it is indicated that these integrals are functions of \mathbf{v} , but also implicitly of the body velocities, \mathbf{v}_b and $\boldsymbol{\omega}_b$, as well. To expose this dependence consider linear approximations of \mathcal{F}_μ and \mathcal{G}_μ about some predicted states, \mathbf{v}^p , \mathbf{v}_b^p , and $\boldsymbol{\omega}_b^p$, which are assumed to be known. These approximations have the form

$$\mathcal{F}_\mu(\mathbf{v}, \mathbf{v}_b, \boldsymbol{\omega}_b) \approx \mathcal{F}_\mu(\mathbf{v}^p, \mathbf{v}_b^p, \boldsymbol{\omega}_b^p) - \mathcal{D}^{vv}(\mathbf{v}_b - \mathbf{v}_b^p) - \mathcal{D}^{v\omega}(\boldsymbol{\omega}_b - \boldsymbol{\omega}_b^p), \quad (17)$$

$$\mathcal{G}_\mu(\mathbf{v}, \mathbf{v}_b, \boldsymbol{\omega}_b) \approx \mathcal{G}_\mu(\mathbf{v}^p, \mathbf{v}_b^p, \boldsymbol{\omega}_b^p) - \mathcal{D}^{\omega v}(\mathbf{v}_b - \mathbf{v}_b^p) - \mathcal{D}^{\omega\omega}(\boldsymbol{\omega}_b - \boldsymbol{\omega}_b^p), \quad (18)$$

where the *added-damping tensors*, \mathcal{D}^{vv} , $\mathcal{D}^{v\omega}$, $\mathcal{D}^{\omega v}$, and $\mathcal{D}^{\omega\omega}$, are 3×3 matrices (assuming three-dimensional flow) defined by

$$\mathcal{D}^{vv} \stackrel{\text{def}}{=} -\frac{\partial \mathcal{F}_\mu}{\partial \mathbf{v}_b}, \quad \mathcal{D}^{v\omega} \stackrel{\text{def}}{=} -\frac{\partial \mathcal{F}_\mu}{\partial \boldsymbol{\omega}_b}, \quad (19)$$

$$\mathcal{D}^{\omega v} \stackrel{\text{def}}{=} -\frac{\partial \mathcal{G}_\mu}{\partial \mathbf{v}_b}, \quad \mathcal{D}^{\omega\omega} \stackrel{\text{def}}{=} -\frac{\partial \mathcal{G}_\mu}{\partial \boldsymbol{\omega}_b}. \quad (20)$$

The approximations in (17) and (18) are sufficient to expose the dependence of the applied forces on the velocities \mathbf{v}_b and $\boldsymbol{\omega}_b$. Note that the added-damping tensors introduced here are an extension of the scalar *added-damping coefficients*, \mathcal{D}^u and \mathcal{D}^ω , obtained in Part I [3] for two model FSI problems.

Exact formulas for the added-damping tensors can be obtained by first noting that the shear stress on the surface of the rigid body, $\boldsymbol{\tau}\mathbf{n}$, appearing in the integrals in (16) can be expressed in terms of the normal derivative of the fluid velocity on the surface and the angular velocity of the rigid body. This form is given in the following theorem.

Theorem 1. *The shear stress of a viscous incompressible fluid with velocity $\mathbf{v}(\mathbf{x}, t)$ and dynamic viscosity μ on the surface of a rigid body with angular velocity $\boldsymbol{\omega}_b(t)$ is given by*

$$\boldsymbol{\tau}\mathbf{n} = \mu \left\{ (\mathbf{I} - \mathbf{n}\mathbf{n}^T) \frac{\partial \mathbf{v}}{\partial n} + \mathbf{n} \times \boldsymbol{\omega}_b \right\}, \quad \mathbf{x} \in \Gamma_b, \quad (21)$$

where \mathbf{I} is the 3×3 identity matrix.

The proof of this theorem is given in [Appendix A](#).

Using (21) to eliminate $\boldsymbol{\tau}\mathbf{n}$ in the integrals in (16) gives

$$\begin{aligned} \mathcal{F}_\mu(\mathbf{v}, \mathbf{v}_b, \boldsymbol{\omega}_b) &= \mu \int_{\Gamma_b} \left\{ (\mathbf{I} - \mathbf{n}\mathbf{n}^T) \frac{\partial \mathbf{v}}{\partial n} + \mathbf{n} \times \boldsymbol{\omega}_b \right\} dS, \\ \mathcal{G}_\mu(\mathbf{v}, \mathbf{v}_b, \boldsymbol{\omega}_b) &= \mu \int_{\Gamma_b} (\mathbf{r} - \mathbf{x}_b) \times \left\{ (\mathbf{I} - \mathbf{n}\mathbf{n}^T) \frac{\partial \mathbf{v}}{\partial n} + \mathbf{n} \times \boldsymbol{\omega}_b \right\} dS, \end{aligned}$$

Define a skew symmetric matrix $[\mathbf{x}]_{\times} \in \mathbb{R}^{3 \times 3}$,

$$[\mathbf{x}]_{\times} \stackrel{\text{def}}{=} \begin{bmatrix} 0 & -x_3 & x_2 \\ x_3 & 0 & -x_1 \\ -x_2 & x_1 & 0 \end{bmatrix},$$

so that the cross product can be rewritten as matrix multiplication,

$$\mathbf{x} \times \mathbf{y} = [\mathbf{x}]_{\times} \mathbf{y}.$$

Therefore, the added-damping tensors in (19) and (20) can be expressed as

$$\mathcal{D}^{vv} = -\mu \int_{\Gamma_b} \left\{ (\mathbf{I} - \mathbf{nn}^T) \frac{\partial}{\partial n} \left(\frac{\partial \mathbf{v}}{\partial \mathbf{v}_b} \right) \right\} dS, \quad (22)$$

$$\mathcal{D}^{v\omega} = -\mu \int_{\Gamma_b} \left\{ (\mathbf{I} - \mathbf{nn}^T) \frac{\partial}{\partial n} \left(\frac{\partial \mathbf{v}}{\partial \boldsymbol{\omega}_b} \right) + [\mathbf{n}]_{\times} \right\} dS, \quad (23)$$

$$\mathcal{D}^{\omega v} = -\mu \int_{\Gamma_b} [\mathbf{r} - \mathbf{x}_b]_{\times} \left\{ (\mathbf{I} - \mathbf{nn}^T) \frac{\partial}{\partial n} \left(\frac{\partial \mathbf{v}}{\partial \mathbf{v}_b} \right) \right\} dS, \quad (24)$$

$$\mathcal{D}^{\omega\omega} = -\mu \int_{\Gamma_b} [\mathbf{r} - \mathbf{x}_b]_{\times} \left\{ (\mathbf{I} - \mathbf{nn}^T) \frac{\partial}{\partial n} \left(\frac{\partial \mathbf{v}}{\partial \boldsymbol{\omega}_b} \right) + [\mathbf{n}]_{\times} \right\} dS, \quad (25)$$

where the derivatives, $\partial_{\mathbf{v}_b} \mathbf{v}$ and $\partial_{\boldsymbol{\omega}_b} \mathbf{v}$, solve certain variations problems as discussed in Section 6. For the typical case, when the rigid body is fully immersed in the fluid, the terms involving $[\mathbf{n}]_{\times}$ in the added-damping tensors (23) and (25) can be evaluated using Gauss's theorem. Assuming that the body surface Γ_b is sufficiently smooth so that the Gauss divergence theorem holds (this is true, roughly, if the surface is piecewise smooth with a finite number of edges and corners [8]), then

$$\int_{\Gamma_b} n_i dS = 0, \quad \text{and} \quad \int_{\Gamma_b} x_i n_j dS = \int_{\Omega_b} \frac{\partial x_i}{\partial x_j} d\mathbf{x} = \delta_{ij} V_b,$$

where V_b is the volume of the rigid body. Therefore, two of the added-damping tensors can be simplified as

$$\mathcal{D}^{v\omega} = -\mu \int_{\Gamma_b} \left\{ (\mathbf{I} - \mathbf{nn}^T) \frac{\partial}{\partial n} \left(\frac{\partial \mathbf{v}}{\partial \boldsymbol{\omega}_b} \right) \right\} dS, \quad (26)$$

$$\mathcal{D}^{\omega\omega} = 2\mu V_b \mathbf{I} - \mu \int_{\Gamma_b} [\mathbf{r} - \mathbf{x}_b]_{\times} \left\{ (\mathbf{I} - \mathbf{nn}^T) \frac{\partial}{\partial n} \left(\frac{\partial \mathbf{v}}{\partial \boldsymbol{\omega}_b} \right) \right\} dS. \quad (27)$$

The four added-damping tensors can be collected in a larger composite tensor, $\mathbf{D}(t) \in \mathbb{R}^{6 \times 6}$, having the form

$$\mathbf{D} \stackrel{\text{def}}{=} \begin{bmatrix} \mathcal{D}^{vv} & \mathcal{D}^{v\omega} \\ \mathcal{D}^{\omega v} & \mathcal{D}^{\omega\omega} \end{bmatrix}. \quad (28)$$

Note that the added-damping tensors change with time as the body rotates according to the formula

$$\mathcal{D}^{\alpha\beta}(t) = R(t) \mathcal{D}^{\alpha\beta}(0) R^T(t), \quad (29)$$

where $R(t)$ is the rotation matrix given in (12). Thus, the integrals defining the entries in $\mathbf{D}(t)$ can be precomputed at $t = 0$, and then (29) can be used to determine $\mathbf{D}(t)$ at later times. We note that the added-damping tensors in two dimensions can be easily derived from the formulae in three dimensions by, for example, considering cylindrical bodies of unit depth in the z -direction (with no top or bottom) in which case the surface integrals will reduce to line integrals. The resulting expressions can then be restricted to two-dimensional motions.

Motivated by the analysis in [3], it is convenient in the AMP-RB algorithm to express the linearizations in (17) and (18) in terms of the body accelerations \mathbf{a}_b and \mathbf{b}_b . This is accomplished by including a factor of the discrete time-step Δt and an additional added-damping parameter β_d ,

$$\mathcal{F}_{\mu}(\mathbf{v}, \mathbf{v}_b, \boldsymbol{\omega}_b) \approx \mathcal{F}_{\mu}(\mathbf{v}^p, \mathbf{v}_b^p, \boldsymbol{\omega}_b^p) - \beta_d \Delta t \mathcal{D}^{vv} (\mathbf{a}_b - \mathbf{a}_b^p) - \beta_d \Delta t \mathcal{D}^{v\omega} (\mathbf{b}_b - \mathbf{b}_b^p), \quad (30)$$

$$\mathcal{G}_{\mu}(\mathbf{v}, \mathbf{v}_b, \boldsymbol{\omega}_b) \approx \mathcal{G}_{\mu}(\mathbf{v}^p, \mathbf{v}_b^p, \boldsymbol{\omega}_b^p) - \beta_d \Delta t \mathcal{D}^{\omega v} (\mathbf{a}_b - \mathbf{a}_b^p) - \beta_d \Delta t \mathcal{D}^{\omega\omega} (\mathbf{b}_b - \mathbf{b}_b^p). \quad (31)$$

As discussed at length in Part I [3], the choice $\beta_d = 1$ lies in a range of values for β_d that yield stable schemes even for massless bodies. As a result that choice is made here for all computations. Finally, note that while the formulas in (22)–(25) are exact, suitable approximations for the AMP-RB algorithm can be obtained by considering discrete variational problems for the derivatives $\partial_{\mathbf{v}_b} \mathbf{v}$ and $\partial_{\boldsymbol{\omega}_b} \mathbf{v}$ appearing in the four integrals. These approximations are discussed in Section 6.

4. The added-mass and added-damping interface conditions

In this section, the interface conditions used in the AMP-RB scheme to account for added-mass and added-damping effects are derived at a continuous level. These conditions are generalizations of the conditions given in Part I [3] for some simplified model problems. A discretization of the interface conditions obtained here is given later in the description of the AMP-RB scheme.

Added-mass effects arise from the contribution of the pressure to the force and torque on the rigid body. To account for these effects and to obtain the proper force-balance for light rigid-bodies, the fluid and solid *accelerations* are matched at the surface of the rigid body. Using (14), this implies

$$D_t \mathbf{v} = \mathbf{a}_b + \mathbf{b}_b \times (\mathbf{r} - \mathbf{x}_b) + \boldsymbol{\omega}_b \times [\boldsymbol{\omega}_b \times (\mathbf{r}(t) - \mathbf{x}_b(t))], \quad \mathbf{r} \in \Gamma_b,$$

where $\mathbf{r}(t)$ denotes a point on the surface of the body and $D_t = \partial_t + \dot{\mathbf{r}} \cdot \nabla$ denotes the total derivative following a point on the surface. Using the momentum equation (1) to eliminate $D_t \mathbf{v}$ leads to the vector *acceleration compatibility condition* given by

$$-\frac{1}{\rho} [\nabla p - \mu \Delta \mathbf{v}] = \mathbf{a}_b + \mathbf{b}_b \times (\mathbf{r} - \mathbf{x}_b) + \boldsymbol{\omega}_b \times [\boldsymbol{\omega}_b \times (\mathbf{r}(t) - \mathbf{x}_b(t))], \quad \mathbf{r} \in \Gamma_b.$$

The normal component of the vector condition can be written in the form

$$\partial_n p = -\rho \mathbf{n}^T \left(\mathbf{a}_b + \mathbf{b}_b \times (\mathbf{r} - \mathbf{x}_b) + \boldsymbol{\omega}_b \times [\boldsymbol{\omega}_b \times (\mathbf{r}(t) - \mathbf{x}_b(t))] \right) + \mu \mathbf{n}^T \Delta \mathbf{v}, \quad \mathbf{r} \in \Gamma_b, \quad (32)$$

where $\mathbf{n} = \mathbf{n}(\mathbf{r}, t)$ is the outward normal to the body.

Added-damping effects arise from the influence of the motion of the rigid body on the integrals in (16) involving the shear stress on the body as discussed in the previous section. The linearizations in (30)–(31) reveal this influence in terms of the accelerations of the body, and these can be added to the interface conditions in (5) and (6). Combining these conditions with the acceleration compatibility condition in (32) leads to the primary AMP-RB interface condition.

AMP Interface Condition. *The AMP-RB interface conditions on the surface of a rigid body $\mathbf{r} \in \Gamma_b$ for the pressure equation (4) are*

$$\partial_n p + \rho \mathbf{n}^T \left(\mathbf{a}_b + \mathbf{b}_b \times (\mathbf{r} - \mathbf{x}_b) \right) = -\rho \mathbf{n}^T \left(\boldsymbol{\omega}_b \times [\boldsymbol{\omega}_b \times (\mathbf{r}(t) - \mathbf{x}_b(t))] \right) + \mu \mathbf{n}^T \Delta \mathbf{v}, \quad (33)$$

$$\left\{ \begin{bmatrix} m_b I_{3 \times 3} & 0 \\ 0 & \mathbf{I}_b \end{bmatrix} + \beta_d \Delta t \mathbf{D} \right\} \begin{bmatrix} \mathbf{a}_b \\ \mathbf{b}_b \end{bmatrix} + \mathbf{F}(p) = - \begin{bmatrix} 0 \\ \boldsymbol{\omega}_b \times \mathbf{I}_b \boldsymbol{\omega}_b \end{bmatrix} + \mathbf{G}(\mathbf{v}) + \beta_d \Delta t \mathbf{D} \begin{bmatrix} \mathbf{a}_b \\ \mathbf{b}_b \end{bmatrix}, \quad (34)$$

where

$$\mathbf{F}(p) \stackrel{\text{def}}{=} \begin{bmatrix} - \int_{\Gamma_b} p \mathbf{n} dS \\ - \int_{\Gamma_b} (\mathbf{r} - \mathbf{x}_b) \times (p \mathbf{n}) dS \end{bmatrix}, \quad \mathbf{G}(\mathbf{v}) \stackrel{\text{def}}{=} \begin{bmatrix} \mathcal{F}_\mu + \mathbf{f}_e \\ \mathcal{G}_\mu + \mathbf{g}_e \end{bmatrix} = \begin{bmatrix} \int_{\Gamma_b} \boldsymbol{\tau} \mathbf{n} dS + \mathbf{f}_e \\ \int_{\Gamma_b} (\mathbf{r} - \mathbf{x}_b) \times (\boldsymbol{\tau} \mathbf{n}) dS + \mathbf{g}_e \end{bmatrix}. \quad (35)$$

Here, Δt is the time-step used in the AMP-RB time-stepping scheme and β_d is the added-damping parameter typically set to one.

In the AMP-RB time-stepping scheme, predicted values for \mathbf{v} , \mathbf{a}_b , \mathbf{b}_b , $\boldsymbol{\omega}_b$ and \mathbf{x}_b are used to evaluate the right-hand sides of the AMP interface conditions in (33) and (34). The fluid pressure p and body accelerations, \mathbf{a}_b and \mathbf{b}_b , are then updated by solving the Poisson equation in (4) together with the AMP interface conditions. Note that the same term involving \mathbf{D} with components $\mathcal{D}^{\alpha\beta}$ appears on both sides of (34). Thus, the components of this interface condition reduce to the conditions in (5) and (6), so that the interface condition is exact for *any* choice of the added-damping tensor \mathbf{D} , including the approximations obtained later in Section 6. The purpose of including the term involving \mathbf{D} in (34) is to cancel the leading contributions to the added-damping embedded in the integrals \mathcal{F}_μ and \mathcal{G}_μ in \mathbf{G} . These contributions now appear on the left-hand side of (34) in the calculation of the body accelerations.

5. The AMP-RB time-stepping algorithm

We now describe a second-order accurate version of the AMP-RB time-stepping algorithm. In this scheme, the fluid variables are computed in a fractional-step manner with the fluid velocity advanced in one stage, followed by an update of the fluid pressure in a subsequent stage. A key element of the algorithm is the AMP-RB interface conditions, which are used to couple the update of the pressure with the calculation of the accelerations of the rigid body. These interface conditions are designed to suppress instabilities due to added-mass and added-damping effects as discussed previously.

Before describing the time-stepping algorithm in detail, let us first introduce some notation. Let \mathbf{x}_i denote the grid-point coordinates on a discrete mesh, where $\mathbf{i} = (i_1, i_2, i_3)$ is a multi-index, and let $t^n = n\Delta t$, $n = 0, 1, 2, 3, \dots$ denote the discrete times in terms of the time-step Δt . The *composite grid* covering the fluid domain, $\Omega(t)$, at time $t = t^n$ is denoted by \mathcal{G}^n . This grid is composed of a collection of component grids, some of which are fitted to the surface of the rigid body and move in time, as described in Section 7. Let $\mathbf{v}_i^n \approx \mathbf{v}(\mathbf{x}_i, t^n)$ and $p_i^n \approx p(\mathbf{x}_i, t^n)$ denote grid functions for the fluid velocity and pressure, respectively, and let $\mathbf{x}_b^n \approx \mathbf{x}_b(t^n)$, $\mathbf{v}_b^n \approx \mathbf{v}_b(t^n)$, etc., denote time-discrete approximations of the rigid-body variables. Let ∇_h and Δ_h denote some appropriate discrete approximations to the gradient and Laplacian operators, respectively; the precise form of these approximations is not important for the present discussion. Let Ω_h denote the set of indices \mathbf{i} in the interior of the fluid grid, Γ_h denote the set of indices \mathbf{i} on the interface, and

$$\mathbf{f}_i^n \stackrel{\text{def}}{=} ((\mathbf{v}_i^n - \mathbf{w}_i^n) \cdot \nabla_h) \mathbf{v}_i^n + \nabla_h p_i^n, \quad (36)$$

denote the advection and pressure terms in the momentum equations, where the *grid velocity*, \mathbf{w}_i^n , is included from the transformation to a moving coordinate system. Finally, denote the state of the rigid body as a vector given by

$$\mathbf{q}_b^n \stackrel{\text{def}}{=} [\mathbf{a}_b^n, \mathbf{b}_b^n, \mathbf{v}_b^n, \boldsymbol{\omega}_b^n, \mathbf{x}_b^n, E_b^n].$$

The AMP-RB time-stepping scheme described in Algorithm 1 is a predictor-corrector-type fractional-step scheme for the fluid velocity and pressure that incorporates the AMP interface conditions coupling the motion of the rigid body. The algorithm involves a set of four procedures, which are given below, and is a generalization of the AMP-RB scheme discussed in detail in Part I [3] for a simplified model problem. The key steps in the algorithm are Steps 3 and 6 where the pressure and body accelerations are computed with the aim to suppress instabilities caused by added-mass and added-damping effects. The correction steps, Steps 5–7, can be repeated any number of times (or omitted completely), but we usually apply these steps once as this increases the stability region of the scheme to allow a larger advection time-step. The velocity correction in Step 8 is optional, although including this step improves the stability of the scheme for added-damping effects, as noted in Part I, and may be needed when these effects are large.

Procedure ($\mathbf{q}_b, \mathcal{G}$) = **predictAndExtrapRigidBody**($\mathbf{q}_b^n, \mathbf{q}_b^{n-1}$)

Predict the accelerations of the rigid body at t^{n+1} using linear extrapolation in time,

$$\mathbf{a}_b = 2\mathbf{a}_b^n - \mathbf{a}_b^{n-1}, \quad \mathbf{b}_b = 2\mathbf{b}_b^n - \mathbf{b}_b^{n-1}.$$

Predict the primary rigid-body degrees-of-freedom at t^{n+1} using a leap-frog scheme in time,

$$\begin{aligned} \mathbf{x}_b &= \mathbf{x}_b^{n-1} + 2\Delta t \mathbf{v}_b^n, & \mathbf{v}_b &= \mathbf{v}_b^{n-1} + 2\Delta t \mathbf{a}_b^n, \\ \boldsymbol{\omega}_b &= \boldsymbol{\omega}_b^{n-1} + 2\Delta t \mathbf{b}_b^n, & E_b &= E_b^{n-1} + 2\Delta t \boldsymbol{\omega}_b^n \times E_b^n, \end{aligned}$$

Algorithm 1 Added-mass partitioned (AMP-RB) scheme

```

// Preliminary body evolution step
1.  $(\mathbf{q}_b^{(e)}, \mathcal{G}^{(e)}) = \text{predictAndExtrapRigidBody}(\mathbf{q}_b^n, \mathbf{q}_b^{n-1})$ 

// Prediction steps
2.  $(\mathbf{v}_i^{(p)}) = \text{advanceFluidVelocity}(\mathbf{q}_b^{(e)}, 2\mathbf{f}_i^n - \mathbf{f}_i^{n-1}, \mathbf{f}_i^n, \mathbf{v}_i^n, \mathcal{G}^{(e)})$ 
3.  $(p_i^{(p)}, \mathbf{a}_b^{(p)}, \mathbf{b}_b^{(p)}) = \text{updatePressureAndBodyAcceleration}(\mathbf{q}_b^{(e)}, \mathbf{v}_i^{(p)}, \mathcal{G}^{(e)})$ 
4.  $(\mathbf{q}_b^{(p)}, \mathcal{G}^{(p)}) = \text{advanceBodyGivenAcceleration}(\mathbf{a}_b^{(p)}, \mathbf{b}_b^{(p)}, \mathbf{q}_b^n)$ 

// Correction steps
5.  $(\mathbf{v}_i^{n+1}) = \text{advanceFluidVelocity}(\mathbf{q}_b^{(p)}, \mathbf{f}_i^{(p)}, \mathbf{f}_i^n, \mathbf{v}_i^n, \mathcal{G}^{(p)})$ 
6.  $(p_i^{n+1}, \mathbf{a}_b^{n+1}, \mathbf{b}_b^{n+1}) = \text{updatePressureAndBodyAcceleration}(\mathbf{q}_b^{(p)}, \mathbf{v}_i^{n+1}, \mathcal{G}^{(p)})$ 
7.  $(\mathbf{q}_b^{n+1}, \mathcal{G}^{n+1}) = \text{advanceBodyGivenAcceleration}(\mathbf{a}_b^{n+1}, \mathbf{b}_b^{n+1}, \mathbf{q}_b^n)$ 

// Fluid-velocity correction step (optional)
8.  $(\mathbf{v}_i^{n+1}) = \text{advanceFluidVelocity}(\mathbf{q}_b^{n+1}, \mathbf{f}_i^{n+1}, \mathbf{f}_i^n, \mathbf{v}_i^n, \mathcal{G}^{n+1})$ 

```

and then update the state of the rigid body at t^{n+1} given by

$$\mathbf{q}_b = [\mathbf{a}_b, \mathbf{b}_b, \mathbf{v}_b, \boldsymbol{\omega}_b, \mathbf{x}_b, E_b].$$

The predicted moving grid at the new time, \mathcal{G} , can now be generated given the position of the body surface $\mathbf{r}(t)$ at $t = t^{n+1}$ determined from (11) and (12) using \mathbf{x}_b and E_b .

Procedure $(\mathbf{v}_i) = \text{advanceFluidVelocity}(\mathbf{q}_b^*, \mathbf{f}_i^*, \mathbf{f}_i^n, \mathbf{v}_i^n, \mathcal{G}^*)$

Advance the fluid velocity with a semi-implicit scheme using the given values \mathbf{f}_i^* and \mathbf{f}_i^n for the advection and pressure gradient terms (36), and setting the fluid velocity on the surface of the rigid body to match that of the body using the given state \mathbf{q}_b^* ,

$$\begin{aligned} \rho \frac{\mathbf{v}_i - \mathbf{v}_i^n}{\Delta t} + \frac{1}{2}\mathbf{f}_i^* + \frac{1}{2}\mathbf{f}_i^n &= \frac{\mu}{2} (\Delta_h \mathbf{v}_i + \Delta_h \mathbf{v}_i^n), & \mathbf{i} \in \Omega_h, \\ \mathbf{v}_i &= \mathbf{v}_b^* + \boldsymbol{\omega}_b^* \times (\mathbf{r}_i^* - \mathbf{x}_b^*), \quad \nabla_h \cdot \mathbf{v}_i = 0, & \text{Extrapolate ghost: } \mathbf{t}_m^T \mathbf{v}_i, \quad \mathbf{i} \in \Gamma_h. \end{aligned}$$

Here the ghost point values for the velocity are determined by the divergence boundary condition together with extrapolation of the tangential components. Appropriate conditions on the velocity are specified on other boundaries, e.g. no-slip conditions on $\partial\Omega \setminus \Gamma_b$.

Procedure $(p_i, \mathbf{a}_b, \mathbf{b}_b) = \text{updatePressureAndBodyAcceleration}(\mathbf{q}_b^*, \mathbf{v}_i^*, \mathcal{G}^*)$

Update the fluid pressure and rigid-body accelerations by solving

$$\Delta_h p_i = -\nabla_h \mathbf{v}_i^* : (\nabla_h \mathbf{v}_i^*)^T, \quad \mathbf{i} \in \Omega_h \cup \Gamma_h,$$

together with the interface conditions⁷

$$\mathbf{n}_i^T \nabla_h p_i + \rho \mathbf{n}_i^T (\mathbf{a}_b + \mathbf{b}_b \times (\mathbf{r}_i^* - \mathbf{x}_b^*)) = -\rho \mathbf{n}_i^T (\boldsymbol{\omega}_b^* \times [\boldsymbol{\omega}_b^* \times (\mathbf{r}_i^* - \mathbf{x}_b^*)]) - \mu \mathbf{n}_i^T (\nabla_h \times \nabla_h \times \mathbf{v}_i^*), \quad \mathbf{i} \in \Gamma_h, \quad (37)$$

$$\left\{ \begin{bmatrix} m_b I_{3 \times 3} & 0 \\ 0 & \mathbf{I}_b \end{bmatrix} + \Delta t \beta_d \mathbf{D}^* \right\} \begin{bmatrix} \mathbf{a}_b \\ \mathbf{b}_b \end{bmatrix} + \mathbf{F}(p_i) = - \begin{bmatrix} 0 \\ \boldsymbol{\omega}_b^* \times \mathbf{I}_b \boldsymbol{\omega}_b^* \end{bmatrix} + \mathbf{G}(\mathbf{v}_i^*) + \Delta t \beta_d \mathbf{D}^* \begin{bmatrix} \mathbf{a}_b^* \\ \mathbf{b}_b^* \end{bmatrix}. \quad (38)$$

Here \mathbf{D}^* is the added damping tensor (28), computed using (29), and \mathbf{F} and \mathbf{G} are defined in (35). Appropriate boundary conditions for pressure are specified on the other boundaries.

Procedure ($\mathbf{q}_b, \mathcal{G}$) = **advanceBodyGivenAcceleration**($\mathbf{a}_b^*, \mathbf{b}_b^*, \mathbf{q}_b^n$)

Use the trapezoidal rule to correct the positions and velocities of the rigid body using the given accelerations \mathbf{a}_b^* and \mathbf{b}_b^* ,

$$\begin{aligned} \mathbf{v}_b &= \mathbf{v}_b^n + \frac{\Delta t}{2} (\mathbf{a}_b^* + \mathbf{a}_b^n), & \boldsymbol{\omega}_b &= \boldsymbol{\omega}_b^n + \frac{\Delta t}{2} (\mathbf{b}_b^* + \mathbf{b}_b^n), \\ \mathbf{x}_b &= \mathbf{x}_b^n + \frac{\Delta t}{2} (\mathbf{v}_b + \mathbf{v}_b^n), & E_b &= E_b^n + \frac{\Delta t}{2} (\boldsymbol{\omega}_b \times E_b^* + \boldsymbol{\omega}_b^n \times E_b^n). \end{aligned}$$

and then update the state of the rigid body at t^{n+1} given by

$$\mathbf{q}_b = [\mathbf{a}_b^*, \mathbf{b}_b^*, \mathbf{v}_b, \boldsymbol{\omega}_b, \mathbf{x}_b, E_b].$$

The moving grid, \mathcal{G} , is corrected using the current position of the body.

6. Discrete and approximate added-damping tensors

In this section we return to the formulas for the added-damping tensors in (22)–(25) and describe an approach to obtain discrete approximations that can be used in the AMP-RB time-stepping scheme. Following the discussion in Part I [3], we begin with a fully-coupled (monolithic) discretization of the governing equations. The discrete equations for the fluid in velocity-pressure form are

$$\rho \left[\frac{\mathbf{v}_i^{n+1} - \mathbf{v}_i^n}{\Delta t} \right] + \frac{3}{2} \mathbf{f}_i^n - \frac{1}{2} \mathbf{f}_i^{n-1} = \mu \left[\alpha \Delta_h \mathbf{v}_i^{n+1} + (1 - \alpha) \Delta_h \mathbf{v}_i^n \right], \quad \mathbf{i} \in \Omega_h, \quad (39)$$

$$\Delta_h p_i^{n+1} = -\nabla_h \mathbf{v}_i^{n+1} : (\nabla_h \mathbf{v}_i^{n+1})^T, \quad \mathbf{i} \in \Omega_h, \quad (40)$$

where \mathbf{f}_i^n is given in (36). Boundary conditions for the discrete velocity, \mathbf{v}_i^{n+1} , and pressure, p_i^{n+1} , on the surface of the rigid body at t^{n+1} are

$$\mathbf{v}_i^{n+1} = \mathbf{v}_b^{n+1} + \boldsymbol{\omega}_b^{n+1} \times (\mathbf{r}_i^{n+1} - \mathbf{x}_b^{n+1}), \quad \mathbf{i} \in \Gamma_h, \quad (41)$$

$$\begin{aligned} (\mathbf{n}_i \cdot \nabla_h) p_i^{n+1} &= \mathbf{n}_i^T \left(\mathbf{a}_b^{n+1} + \mathbf{b}_b^{n+1} \times (\mathbf{r}_i^{n+1} - \mathbf{x}_b^{n+1}) \right. \\ &\quad \left. + \boldsymbol{\omega}_b^{n+1} \times (\boldsymbol{\omega}_b^{n+1} \times (\mathbf{r}_i^{n+1} - \mathbf{x}_b^{n+1})) + \nu \Delta_h \mathbf{v}_i^{n+1} \right), \quad \mathbf{i} \in \Gamma_h, \end{aligned} \quad (42)$$

⁷The term $\Delta \mathbf{v}$ in the boundary condition (37) has been replaced by $-\nabla \times \nabla \times \mathbf{v}$ to avoid a viscous time-step restriction, see for example, [9].

These boundary conditions involve the discrete quantities, \mathbf{x}_b^{n+1} , \mathbf{v}_b^{n+1} , etc., of the body which are determined by the following discretization of the Euler-Newton equations:

$$m_b \mathbf{a}_b^{n+1} = \sum_{\mathbf{i} \in \Gamma_h} \left\{ \mathbf{n}_i^T (-p_i^{n+1} \mathbf{I} + \mathbf{T}_i^{n+1}) \Delta S_i \right\} + \mathbf{f}_e(t^{n+1}), \quad (43)$$

$$\mathbf{I}_b \mathbf{b}_b^{n+1} + \boldsymbol{\omega}_b^{n+1} \times \mathbf{I}_b \boldsymbol{\omega}_b^{n+1} = \sum_{\mathbf{i} \in \Gamma_h} \left\{ (\mathbf{r}_i^{n+1} - \mathbf{x}_b^{n+1}) \times (-p_i^{n+1} \mathbf{n}_i + \mathbf{T}_i^{n+1}) \Delta S_i \right\} + \mathbf{g}_e(t^{n+1}), \quad (44)$$

$$\frac{\mathbf{v}_b^{n+1} - \mathbf{v}_b^n}{\Delta t} = \bar{\alpha} \mathbf{a}_b^{n+1} + (1 - \bar{\alpha}) \mathbf{a}_b^n, \quad (45)$$

$$\frac{\boldsymbol{\omega}_b^{n+1} - \boldsymbol{\omega}_b^n}{\Delta t} = \bar{\alpha} \mathbf{b}_b^{n+1} + (1 - \bar{\alpha}) \mathbf{b}_b^n, \quad (46)$$

$$\frac{\mathbf{x}_b^{n+1} - \mathbf{x}_b^n}{\Delta t} = \bar{\alpha} \mathbf{v}_b^{n+1} + (1 - \bar{\alpha}) \mathbf{v}_b^n, \quad (47)$$

$$\frac{E_b^{n+1} - E_b^n}{\Delta t} = \bar{\alpha} (\boldsymbol{\omega}_b^{n+1} \times E_b^{n+1}) + (1 - \bar{\alpha}) (\boldsymbol{\omega}_b^n \times E_b^n), \quad (48)$$

where \mathbf{T}_i^{n+1} is a discrete approximation of the shear stress, $\boldsymbol{\tau} \mathbf{n}$, on the surface of the body, $\mathbf{i} \in \Gamma_h$. The discretization of the fluid also requires boundary conditions for $\mathbf{i} \in \partial\Omega_h \setminus \Gamma_h$, but the choice of these boundary conditions is not important for the present discussion. The parameters α in (39) and $\bar{\alpha}$ in (45)–(48) are time-stepping parameters, and typical values are taken to be 1/2 corresponding to the trapezoidal rule. The symbol, ΔS_i , in (43) and (44) denotes the area weights in the quadrature-rule approximation of the surface integrals on the body.

Discrete approximations for the derivatives, $\partial_{\mathbf{v}_b} \mathbf{v}$ and $\partial_{\boldsymbol{\omega}_b} \mathbf{v}$, that appear in the formulas for the added-damping tensors in (22)–(25) can be obtained by solving variational problems derived from the discretization of the governing equations. The key equations among the coupled set of equations are (39) and (41) for \mathbf{v}_i^{n+1} . Let $\mathbf{W}_i^v \in \mathbb{R}^{3 \times 3}$ and $\mathbf{W}_i^\omega \in \mathbb{R}^{3 \times 3}$ given by

$$\mathbf{W}_i^v \stackrel{\text{def}}{=} \frac{\partial \mathbf{v}_i^{n+1}}{\partial \mathbf{v}_b^{n+1}}, \quad \mathbf{W}_i^\omega \stackrel{\text{def}}{=} \frac{\partial \mathbf{v}_i^{n+1}}{\partial \boldsymbol{\omega}_b^{n+1}},$$

denote discrete approximations of the derivatives, $\partial_{\mathbf{v}_b} \mathbf{v}$ and $\partial_{\boldsymbol{\omega}_b} \mathbf{v}$. Taking the derivative of the equations with respect to \mathbf{v}_b^{n+1} (with the other discrete quantities for the body held fixed) shows that \mathbf{W}_i^v satisfies a discrete Helmholtz problem given by

$$\frac{\rho}{\Delta t} \mathbf{W}_i^v = \mu \alpha \Delta_h \mathbf{W}_i^v, \quad \mathbf{i} \in \Omega_h, \quad (49)$$

$$\mathbf{W}_i^v = \mathbf{I}, \quad \mathbf{i} \in \Gamma_h, \quad (50)$$

where \mathbf{I} is the 3×3 identity and with homogeneous boundary conditions for \mathbf{W}_i^v on $\mathbf{i} \in \partial\Omega_h \setminus \Gamma_h$ of the same form as that imposed for (39). Similarly, taking the derivative with respect to $\boldsymbol{\omega}_b^{n+1}$ gives

$$\frac{\rho}{\Delta t} \mathbf{W}_i^\omega = \mu \alpha \Delta_h \mathbf{W}_i^\omega, \quad \mathbf{i} \in \Omega_h, \quad (51)$$

$$\mathbf{W}_i^\omega = -[\mathbf{r}_i^{n+1} - \mathbf{x}_b^{n+1}]_\times, \quad \mathbf{i} \in \Gamma_h, \quad (52)$$

with homogeneous boundary conditions for \mathbf{W}_i^ω on $\mathbf{i} \in \partial\Omega_h \setminus \Gamma_h$ as before. Assuming that \mathbf{W}_i^v and \mathbf{W}_i^ω can be found, discrete forms corresponding to (22), (24), (26), and (27) are

$$\mathcal{D}_h^{vv} \stackrel{\text{def}}{=} -\mu \sum_{\mathbf{i} \in \Gamma_h} \{ (\mathbf{I} - \mathbf{n}_i \mathbf{n}_i^T) D_{nh} \mathbf{W}_i^v \} \Delta S_i, \quad (53)$$

$$\mathcal{D}_h^{v\omega} \stackrel{\text{def}}{=} -\mu \sum_{\mathbf{i} \in \Gamma_h} \{ (\mathbf{I} - \mathbf{n}_i \mathbf{n}_i^T) D_{nh} \mathbf{W}_i^\omega \} \Delta S_i, \quad (54)$$

$$\mathcal{D}_h^{\omega v} \stackrel{\text{def}}{=} -\mu \sum_{\mathbf{i} \in \Gamma_h} [\mathbf{r}_i^{n+1} - \mathbf{x}_b^{n+1}]_\times \{ (\mathbf{I} - \mathbf{n}_i \mathbf{n}_i^T) D_{nh} \mathbf{W}_i^v \} \Delta S_i, \quad (55)$$

$$\mathcal{D}_h^{\omega\omega} \stackrel{\text{def}}{=} 2\mu V_b \mathbf{I} - \mu \sum_{\mathbf{i} \in \Gamma_h} [\mathbf{r}_i^{n+1} - \mathbf{x}_b^{n+1}]_\times \{ (\mathbf{I} - \mathbf{n}_i \mathbf{n}_i^T) D_{nh} \mathbf{W}_i^\omega \} \Delta S_i, \quad (56)$$

where D_{nh} is a discrete approximation of the normal derivative on the surface of the rigid body.

While it is possible to evaluate the added-damping tensors in (53)–(56) by solving the discrete Helmholtz problems for \mathbf{W}_i^v and \mathbf{W}_i^ω , this is considered to be too much effort when only approximations to these tensors are needed for the AMP-RB time-stepping scheme. Following the approximations made in the model-problem analysis in Part I [3], it is postulated that the normal derivatives of \mathbf{W}_i^v and \mathbf{W}_i^ω on the surface of the rigid body can be approximated by

$$D_{nh} \mathbf{W}_i^v \approx -\frac{1}{\Delta n_i} \mathbf{I}, \quad D_{nh} \mathbf{W}_i^\omega \approx \frac{1}{\Delta n_i} [\mathbf{r}_i^{n+1} - \mathbf{x}_b^{n+1}]_\times, \quad \mathbf{i} \in \Gamma_h, \quad (57)$$

where Δn_i is the *added-damping length-scale* parameter given by

$$\Delta n_i \stackrel{\text{def}}{=} \frac{\Delta s_{n,i}}{1 - e^{-\delta_i}}, \quad \delta_i \stackrel{\text{def}}{=} \frac{\Delta s_{n,i}}{\sqrt{\alpha\nu\Delta t}}, \quad \mathbf{i} \in \Gamma_h. \quad (58)$$

Here, $\Delta s_{n,i}$ is the mesh spacing in the normal direction, α is the time-stepping parameter in (39), and $\nu = \mu/\rho$ is the kinematic viscosity. As noted in Part I, Δn_i varies with δ_i , which is the ratio of the mesh spacing in the normal direction to a *viscous* grid spacing, and it takes the limiting values

$$\Delta n_i \sim \begin{cases} \sqrt{\alpha\nu\Delta t} & \text{for } \delta_i \rightarrow 0, \\ \Delta s_{n,i} & \text{for } \delta_i \rightarrow \infty. \end{cases}$$

Using the approximations in (57) with Δn_i given in (58) leads to the simplified added-damping tensors

$$\tilde{\mathcal{D}}_h^{vv} \stackrel{\text{def}}{=} \mu \sum_{\mathbf{i} \in \Gamma_h} \frac{1}{\Delta n_i} (\mathbf{I} - \mathbf{n}_i \mathbf{n}_i^T) \Delta S_i, \quad (59)$$

$$\tilde{\mathcal{D}}_h^{v\omega} \stackrel{\text{def}}{=} \mu \sum_{\mathbf{i} \in \Gamma_h} \frac{1}{\Delta n_i} (\mathbf{I} - \mathbf{n}_i \mathbf{n}_i^T) [\mathbf{r}_i^{n+1} - \mathbf{x}_b^{n+1}]_\times^T \Delta S_i, \quad (60)$$

$$\tilde{\mathcal{D}}_h^{\omega v} \stackrel{\text{def}}{=} \mu \sum_{\mathbf{i} \in \Gamma_h} \frac{1}{\Delta n_i} [\mathbf{r}_i^{n+1} - \mathbf{x}_b^{n+1}]_\times (\mathbf{I} - \mathbf{n}_i \mathbf{n}_i^T) \Delta S_i, \quad (61)$$

$$\tilde{\mathcal{D}}_h^{\omega\omega} \stackrel{\text{def}}{=} \mu \sum_{\mathbf{i} \in \Gamma_h} \frac{1}{\Delta n_i} [\mathbf{r}_i^{n+1} - \mathbf{x}_b^{n+1}]_\times (\mathbf{I} - \mathbf{n}_i \mathbf{n}_i^T) [\mathbf{r}_i^{n+1} - \mathbf{x}_b^{n+1}]_\times^T \Delta S_i. \quad (62)$$

The term involving the volume of body has been dropped from the approximations in (62) since this term will generally be small compared to the term that was kept.

The approximate composite added-damping tensor given by

$$\tilde{\mathbf{D}} \stackrel{\text{def}}{=} \begin{bmatrix} \tilde{\mathcal{D}}_h^{vv} & \tilde{\mathcal{D}}_h^{v\omega} \\ \tilde{\mathcal{D}}_h^{\omega v} & \tilde{\mathcal{D}}_h^{\omega\omega} \end{bmatrix}, \quad (63)$$

is used in the AMP-RB time-stepping scheme. We note that $\tilde{\mathbf{D}}$ is symmetric and positive semi-definite, and thus it provides a damping contribution to the calculation of the accelerations of the rigid body in (38). We note also that the added-damping tensors in $\tilde{\mathbf{D}}$ need only be computed for the problem configuration at the initial time $t^n = 0$, since the tensors at later times can be computed based on the rotation of the rigid body according to (29).

7. Numerical approach using moving composite grids

Our numerical approach for the solution of the equations governing an FSI initial-boundary-value problem is based on the use of moving (and possibly deforming) composite grids. This flexible approach enables the use of efficient structured grids for complex geometry and provides smooth, high-quality grids for moving grid problems even as the geometry undergoes large changes. We have previously applied this approach to the coupling of compressible flows and rigid bodies [4, 10], compressible flows with deforming bodies in [11, 12], and incompressible flows with rigid bodies [5] and deforming beams [13].

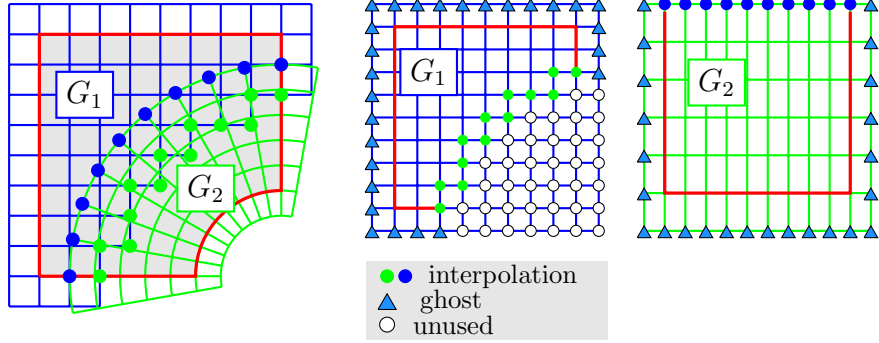


Figure 2: Left: an overlapping grid consisting of two structured curvilinear component grids, $\mathbf{x} = G_1(\mathbf{r})$ and $\mathbf{x} = G_2(\mathbf{r})$. Middle and right: component grids for the square and annular grids in the unit square parameter space \mathbf{r} . Grid points are classified as discretization points, interpolation points or unused points. Ghost points are used to apply boundary conditions.

An overlapping grid, \mathcal{G} , consists of a set of structured component grids, $\{G_g\}$, $g = 1, \dots, \mathcal{N}$, that covers the fluid domain, $\Omega(t)$, and overlap where the component grids meet, see Figure 2. Discrete solutions defined on different grids are matched by interpolation at the *interpolation points*; for the second-order accurate computations performed here, a tensor-product Lagrange interpolation formula is used (i.e. quadratic interpolation using a three-point stencil in each direction). Typically, boundary-fitted curvilinear grids are used near the boundaries (rigid-body surfaces and external boundaries), while one or more background Cartesian grids are used to handle the bulk of the fluid domain. Each component grid is a logically rectangular, curvilinear grid in n_d space dimensions, and is defined by a smooth mapping from parameter space \mathbf{r} (the unit square or cube) to physical space \mathbf{x} ,

$$\mathbf{x} = \mathbf{G}(\mathbf{r}, t), \quad \mathbf{r} \in [0, 1]^{n_d}, \quad \mathbf{x} \in \mathbb{R}^{n_d}.$$

For the present FSI problem, there are usually one or more background grids which are static, while boundary-fitted grids attached to the boundary of the rigid body move over time. The Navier-Stokes equations for the fluid are transformed to the unit-square reference coordinates, \mathbf{r} , using the chain rule. On moving grids, the equations are transformed to a moving coordinate system which introduces the grid velocity into the advection terms as indicated in (36). The resulting equations are then discretized using standard finite-difference approximations for the derivatives with respect to \mathbf{r} . Second-order accurate approximations are used in the present implementation of the time-stepping scheme. For more details on the discretization approach see [1, 4, 13].

Time-step determination. The discrete time-step Δt is generally determined by a CFL-type stability condition based on the advection terms in the fluid momentum equations. The viscous terms are treated implicitly so that there is no stability constraint on Δt arising from these terms. A maximum value for the time-step is also enforced in case the advection terms are small, and this maximum value is often taken to be proportional to the grid spacing (in non-dimensional variables). An additional consideration when choosing the time-step for the AMP-RB scheme is that since the entries in the added-damping tensors depend on Δt (through the factor $\sqrt{\nu\Delta t}$), it is helpful if Δt varies slowly as the simulation progresses. It has been found that if Δt jumps by a significant fraction, e.g. by a factor of two, then for difficult problems with very light bodies, the body acceleration may also experience a small jump (as can be seen, for example, in Figure 9). This jump is local in time and the acceleration recovers after a few time-steps but this can be avoided by either enforcing that Δt varies smoothly, or by adjusting the form of the added-damping coefficients so that these vary smoothly in time.

8. Numerical Results

Numerical results are now presented that demonstrate the stability and accuracy properties of the AMP-RB scheme as implemented using moving overlapping grids⁸. The first problem involves the one-dimensional motion of a piston in a rectangular fluid chamber while the second problem involves the rotation of a solid disk in an annular fluid chamber. These problems are motivated by two of the model problems discussed in Part I [3]. The first problem highlights added-mass effects while the second problem isolates the effects of added-damping. Unlike the model problems considered in Part I, the present problems consider finite amplitude translations and rotations, and overlapping grids are used to handle the moving geometry. Exact solutions are available for both problems, and these solution can be used to assess the stability and accuracy of the general AMP-RB scheme.

Subsequently, four other challenging problems are considered to illustrate the behaviour of the scheme. In the first case, a zero-mass cylindrical body moves within a fluid-filled channel. This problem is designed to provide a clean benchmark problem for evaluating the stability and accuracy of the AMP-RB scheme when both added-mass and added-damping effects are important. Convergence rates are computed from a self-convergence grid refinement study. The next problem considers a standard test problem examined in the literature consisting of a moderately-heavy cylindrical-body that falls, under gravity, in a fluid channel. This problem is used to check the results of the AMP-RB scheme with results from other schemes. The third of these four problems involves a light rectangular-shaped body rising under buoyancy forces to the top of a closed fluid chamber. This problem demonstrates the need for added-mass corrections, and also the need for the added-damping corrections of the AMP-RB scheme for the case of a non-cylindrically-shaped body. For non-cylindrical bodies, one might posit (incorrectly, it turns out) that any finite-size added-mass corrections would be sufficient to stabilize the scheme, without the need for added-damping corrections, since added-mass effects are proportional to changes in the acceleration of the body while added-damping effects are proportional to changes in the velocity; the latter generally being $O(\Delta t)$ smaller than the former. Despite this intuition, it is found in practice that added-damping effects must be properly treated to maintain stability of the scheme. In the last problem, the interaction between two rectangular-shaped bodies, one rising and one falling, in a rectangular fluid chamber is simulated to demonstrate the performance of the scheme with multiple bodies in close proximity.

8.1. One-dimensional motion of a piston and a rectangular fluid chamber

Consider the horizontal motion of a two-dimensional rigid-body (a *piston*) located at one end of a rectangular channel of fluid as shown in Figure 3. The problem is posed with initial conditions and boundary conditions so that an exact solution exists which only depends on the horizontal coordinate x and on time t . The pressure in the fluid provides a force on the rigid-body, which implies the presence of added-mass effects, whereas there are no forces due to viscous shear for this problem so that added-damping effects are negligible. Thus, this FSI problem provides a good test of the added-mass properties of the AMP-RB scheme. Note that although the exact solution for this problem does not depend on y , the numerical solution of the full incompressible Navier-Stokes equations in two dimensions is computed on general moving grids to verify the overall approach.

For this piston problem, the fluid occupies the rectangular channel $\Omega(t) = [x_I(t), L] \times [0, H]$, where $x_I(t)$ is the position of the interface between the fluid and solid, L is the position of the right end of the channel, and H is the height of the channel. The rigid body, located at the left end of the fluid channel, has mass m_b , width W_b and height $H_b = H$. The interface condition on the fluid at the piston face is the velocity matching condition in (15). The boundary conditions on the top and bottom of the fluid channel are slip-walls (equivalent to symmetry conditions), while the condition on the fluid at $x = L$ is taken to be

$$p(L, y, t) = p_L(t), \quad v_2(L, y, t) = 0, \quad y \in [0, H], \quad t > 0,$$

where $p_L(t)$ is a given applied pressure. The solution for the body velocity $\mathbf{v}_b = (v_{1,b}, v_{2,b})^T$, fluid velocity

⁸The examples presented in this section are available with the Overture software at [overtureFramework.org](http://overtureframework.org).

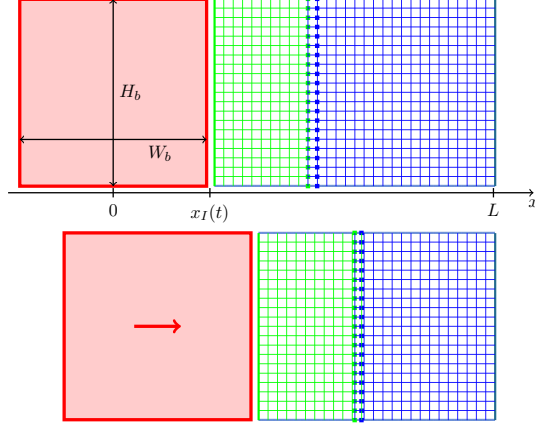


Figure 3: Composite grids for a piston adjacent to a fluid channel. Grids are shown at two times. The green fluid grid adjacent to the piston moves over time. The blue background grid remains fixed.

$\mathbf{v} = (v_1, v_2)^T$ and fluid pressure p is given by

$$v_{1,b}(t) = \int_0^t \frac{-H p_L(\tau) d\tau}{m_b + M_a(\tau)} + v_{1,b}(0), \quad (64)$$

$$p(x, t) = p_L(t) + \left(\frac{L - x}{L - x_I(t)} \right) \frac{-p_L(t)}{m_b/M_a(t) + 1}, \quad (65)$$

$$v_1(t) = v_{1,b}(t), \quad (66)$$

and $v_2 = v_{2,b} = 0$. Here, the horizontal position of the body centre and interface are given by

$$x_b(t) = \int_0^t v_{1,b}(\tau) d\tau + x_b(0), \quad x_I(t) = x_b(t) + W_b/2, \quad (67)$$

and the *added-mass* is determined analytically as

$$M_a(t) = \rho H(L - x_I(t)). \quad (68)$$

The solution in (64)–(68) is an extension of the one for the added-mass model problem in Part I [3]. Here, however, there is no small-amplitude linearization about a fixed interface position, $x_I(t) = 0$, as was done in Part I. While the solution can be determined from a given applied pressure and initial states, $x_b(0)$ and $v_{1,b}(0)$, it is simpler to choose $x_b(t)$ and $v_{1,b}(t) = \dot{x}_b(t)$, and then back out $p_L(t)$ and $p(x, t)$ using (64) and (65), respectively. Following this approach, we set

$$x_b(t) = \alpha_b \sin(2\pi t), \quad \alpha_b = 1/4,$$

to determine solutions for various choices of the parameters in the verification tests below.

Numerical solutions are computed for the piston problem using the composite grid, denoted by $\mathcal{G}_p^{(j)}$, with resolution factor j . As illustrated in Figure 3, the grid consists of two component grids. The first is a body-fitted rectangular grid (green in the figure) of fixed width $1/2$ and height $H = 1$, which is attached to the right face of the rigid body. This moving grid overlaps with a static Cartesian background grid (blue in the figure) covering the region, $[-3/4, L] \times [0, H]$ with $L = 3/2$, which covers the remaining portion of the fluid channel. The grid spacing for both component grids is uniform and chosen to be $h^{(j)} = 1/(10j)$ in each direction. The width and height of the rigid body are taken to be $W_b = H_b = 1$ so that $m_b = \rho_b$, where ρ_b is the density of the solid. The density of the fluid is taken to be $\rho = 1$ and its viscosity is $\mu = 0.1$. In our numerical tests, the density of the fluid is held fixed, while the density of the solid is varied to study the effects of added mass.

Figure 4 shows a time history of the position, velocity and acceleration of the rigid body, together with the errors, as computed with the AMP-RB scheme using the grid $\mathcal{G}_p^{(4)}$ and $\Delta t = 10^{-2}$. Results are shown

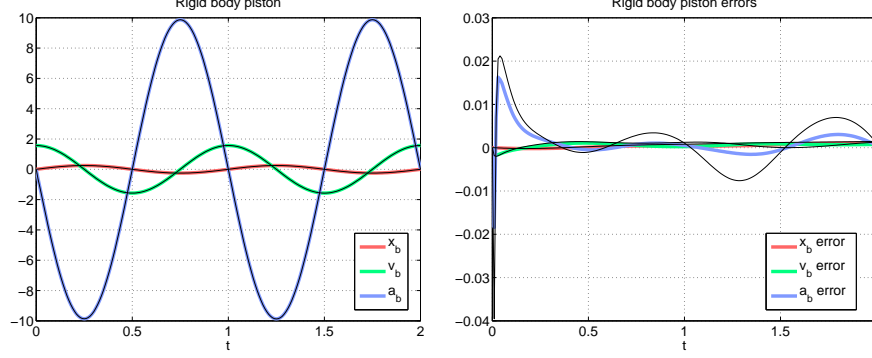


Figure 4: Computed piston motion and errors for $\rho_b = 1$ (coloured lines) and $\rho_b = .01$ (black lines). Results for $\mathcal{G}_p^{(4)}$.

| Piston motion, $\rho_b = 10$ | | | | | | | | | | |
|------------------------------|---------|---|---------|-----|-------------|-----|-------------|-----|-------------|---|
| $h^{(j)}$ | E_j^p | r | E_j^v | r | $E_j^{x_b}$ | r | $E_j^{v_b}$ | r | $E_j^{a_b}$ | r |
| 1/10 | 1.3e-3 | | 9.9e-3 | | 3.7e-2 | | 9.9e-3 | | 1.2e-4 | |
| 1/20 | 4.4e-5 | - | 2.1e-3 | 4.6 | 9.1e-3 | 4.1 | 2.1e-3 | 4.6 | 4.3e-6 | - |
| 1/40 | 5.4e-8 | - | 5.3e-4 | 4.1 | 2.3e-3 | 3.9 | 5.3e-4 | 4.1 | 4.6e-9 | - |
| 1/80 | 4.7e-10 | - | 1.3e-4 | 4.0 | 6.0e-4 | 3.9 | 1.3e-4 | 4.0 | 9.8e-13 | - |
| rate | - | | 2.07 | | 1.98 | | 2.07 | | - | |

| Piston motion, $\rho_b = 1$ | | | | | | | | | | |
|-----------------------------|---------|---|---------|-----|-------------|-----|-------------|-----|-------------|---|
| $h^{(j)}$ | E_j^p | r | E_j^v | r | $E_j^{x_b}$ | r | $E_j^{v_b}$ | r | $E_j^{a_b}$ | r |
| 1/10 | 1.3e-4 | | 4.8e-2 | | 4.6e-2 | | 4.8e-2 | | 1.1e-4 | |
| 1/20 | 1.1e-6 | - | 9.9e-3 | 4.8 | 1.1e-2 | 4.3 | 9.9e-3 | 4.8 | 5.7e-7 | - |
| 1/40 | 8.7e-9 | - | 2.4e-3 | 4.1 | 2.7e-3 | 4.0 | 2.4e-3 | 4.1 | 1.1e-9 | - |
| 1/80 | 7.8e-12 | - | 6.1e-4 | 4.0 | 6.9e-4 | 3.9 | 6.1e-4 | 4.0 | 7.5e-13 | - |
| rate | - | | 2.09 | | 2.02 | | 2.09 | | - | |

| Piston motion, $\rho_b = .001$ | | | | | | | | | | |
|--------------------------------|---------|---|---------|-----|-------------|-----|-------------|-----|-------------|---|
| $h^{(j)}$ | E_j^p | r | E_j^v | r | $E_j^{x_b}$ | r | $E_j^{v_b}$ | r | $E_j^{a_b}$ | r |
| 1/10 | 6.4e-5 | | 8.3e-2 | | 5.5e-2 | | 8.3e-2 | | 5.1e-4 | |
| 1/20 | 3.3e-6 | - | 1.7e-2 | 4.9 | 1.3e-2 | 4.4 | 1.7e-2 | 4.8 | 3.1e-5 | - |
| 1/40 | 2.5e-8 | - | 4.2e-3 | 4.1 | 3.1e-3 | 4.0 | 4.2e-3 | 4.1 | 2.8e-8 | - |
| 1/80 | 4.2e-10 | - | 1.0e-3 | 4.0 | 8.0e-4 | 3.9 | 1.0e-3 | 4.0 | 1.5e-12 | - |
| rate | - | | 2.10 | | 2.03 | | 2.10 | | - | |

Table 1: Piston motion. Maximum errors and estimated convergence rates at $t = 1$ computed using the AMP-RB scheme for a heavy, $\rho_b = 10$, medium, $\rho_b = 1$, and very light, $\rho_b = 0.001$, moving piston. The column labeled "r" provides the ratio of the errors at the current grid spacing to that on the next coarser grid.

for a medium-light body with $\rho_b = 1$ (coloured curves) and a very light body $\rho_b = 0.01$ (black curves). The AMP-RB scheme remains stable for both cases, and that the solution curves for $x_b(t)$, $v_{1,b}(t)$ and $a_{1,b}(t)$ for each value of ρ_b are in good agreement with the exact solution. The observed stability behaviour of the AMP-RB scheme agrees with the analysis in Part I for an added-mass model problem (linearized about a fixed interface position). For the model problem, it was found that the AMP-RB scheme is stable for any ratio of the mass of the body to that of the added mass of the fluid. An analysis of a traditional-partitioned (TP) scheme (with no sub-time-step iterations) for the same model problem found that the TP scheme is stable if and only if $m_b > M_a$. For the present piston problem, the interface position varies with time so that the added mass given in (68) varies with time as well. However, a condition for stability of the TP scheme can be estimated as $m_b > \max(M_a(t)) = 5/4$. As a check, we find that the TP scheme is unstable for calculations using $\mathcal{G}_p^{(4)}$ and $\Delta t = 10^{-2}$ if $\rho_b = m_b \approx 1.5$ and smaller. This result is in reasonable agreement with the estimate.

To assess the accuracy of the AMP-RB scheme, errors are computed on a sequence of grids of increasing

resolution. The time-step is chosen as $\Delta t_j = 1/(10j)$ for $\mathcal{G}_p^{(j)}$ and the equations are integrated to $t_{\text{final}} = 1$. Table 1 presents the results of this grid refinement study for a heavy, medium and light body. The tables show the max-norm errors and estimated convergence rates computed by a least-squares fit to the logarithm of the error. The max-norm error of component q for a calculation using grid $\mathcal{G}_p^{(j)}$ is denoted by E_j^q . For vector quantities such as \mathbf{v} , the corresponding error $E_j^{\mathbf{v}}$ is the maximum taken over all components of the vector. The results show that the scheme is second-order accurate in the fluid velocity, body velocity and body position. The fluid pressure and rigid-body acceleration converge more rapidly for this simple problem since the second-order accurate approximation to the pressure equation is exact for a solution with linear variation in x .

8.2. Rotating disk in an annular fluid chamber

In this section the rotating disk-in-a-disk problem described in Part I [3] is solved using moving overlapping grids to verify the accuracy and stability of the AMP-RB scheme. The geometry of the two-dimensional problem is shown in Figure 5. An annular fluid chamber is bounded by a rotating solid disk of radius $r = r_1$ and a static wall at $r = r_2$. The disk has uniform density ρ_b so that its moment of inertia (for rotation in the plane) is $I_b = \rho_b \pi r_1^4 / 2$. An exact solution for the case when the rigid body rotates about its centre is given in Part I. The solution for the fluid velocity and pressure is given in terms of the polar coordinates (r, θ) by

$$\mathbf{v}(r, \theta, t) = v_\theta(r, t) \begin{bmatrix} -\sin \theta \\ \cos \theta \end{bmatrix}, \quad p(r, t) = \rho \int_{r_1}^r \frac{[v_\theta(s, t)]^2}{s} ds + p_0,$$

where p_0 is a constant and

$$v_\theta(r, t) = \alpha_b \left[\frac{J_1(\lambda r) Y_1(\lambda r_2) - J_1(\lambda r_2) Y_1(\lambda r)}{J_1(\lambda r_1) Y_1(\lambda r_2) - J_1(\lambda r_2) Y_1(\lambda r_1)} \right] e^{-\lambda^2 \nu t},$$

is the circumferential component of the velocity. Here, J_1 and Y_1 are Bessel functions of order one, $\nu = \mu/\rho$ is the kinematic viscosity of the fluid, α_b is the velocity at $r = r_1$ and $t = 0$, and λ is a constant determined by the matching conditions at the interface with the rigid body (see Part I). The angular velocity of the rigid body is given by

$$\omega_b(t) = \frac{v_\theta(r_1, t)}{r_1} = \frac{\alpha_b e^{-\lambda^2 \nu t}}{r_1},$$

where ω_b corresponds to the third component of the angular velocity vector $\boldsymbol{\omega}_b$. Note that the solution exhibits viscous shear at the surface of the rigid body so that this problem provides a good test of the stability of the AMP-RB scheme when added-damping effects are important. Added-mass effects are negligible for this problem since the fluid pressure is uniform along the surface of the rigid body.

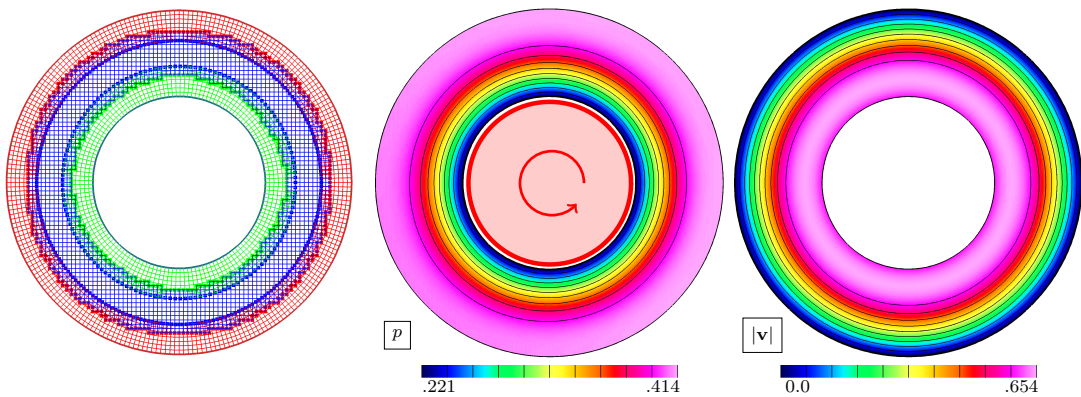


Figure 5: Left: Coarse composite-grid $\mathcal{G}_{\text{rd}}^{(2)}$ for a solid disk immersed in a disk of an incompressible fluid. The green fluid grid adjacent to the rigid disk (solid red) moves in time. The red and blue fluid grids remain fixed. Computed pressure (middle) and speed (right) at $t = 1.0$ on grid $\mathcal{G}_{\text{rd}}^{(4)}$.

Numerical solutions are computed using a composite grid for the annular fluid domain, denoted by $\mathcal{G}_{\text{rd}}^{(j)}$, as shown in Figure 5. The composite grid consists of two annular boundary-fitted component grids and one background Cartesian grid (blue). The inner annular grid (green) is attached to, and moves with, the surface of the rigid body at $r_1 = 1$, while the outer annular grid (red) is fixed to the static outer boundary of the fluid domain at $r_2 = 2$. Both annular grids have radial extent equal to 0.3, and the representative grid spacing is $h^{(j)} = 1/(10j)$ for all component grids in each of their coordinate directions. The initial conditions are taken from the exact solution (with $p_0 = 0$), no-slip boundary conditions are applied at $r = r_2$, and interface matching conditions are applied at the surface of the rigid body, $r = r_1$. The fluid density and viscosity are taken to be $\rho = 1$ and $\mu = 0.1$ for all calculations in this section. Note that the exact solution contains only rotations of the body, while the numerical solution allows both rotational and translational motions of the body.

Figure 5 shows contours of the pressure, p , and speed, $|\mathbf{v}|$, at $t = 1.0$ for the case of a light body with $\rho_b = 0.01$ and for $\alpha_b = 1$. The solution is computed using the AMP-RB scheme with velocity correction on the composite grid $\mathcal{G}_{\text{rd}}^{(4)}$ with $\beta_d = 1$ and Δt determined by the advection time-step restriction. The pressure is seen to depend only on the radius r and the motion of the body is dominated by rotation, in agreement with the exact solution. Even though the body is light there are no instabilities due to added-damping effects, as predicted by the stability analysis in Part I.

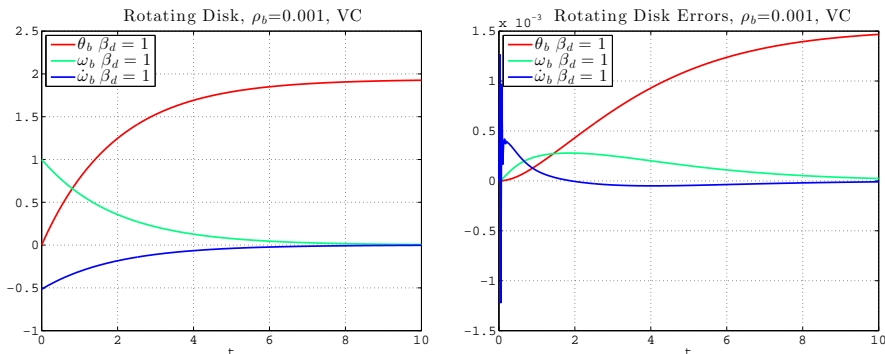


Figure 6: Rotating disk. Rigid-body rotation-angle, angular velocity and angular acceleration for the rotation of a very light rigid disk, $\rho_b = 0.001$, using grid $\mathcal{G}_{\text{rd}}^{(4)}$ and $\Delta t = .05$. Left: solutions. Right: errors.

Figure 6 shows the time history of the rotation angle θ_b , velocity ω_b , and acceleration $\dot{\omega}_b$, of the rigid body, from a calculation of very light rigid-body with $\rho_b = 10^{-3}$. A plot of the errors in these quantities is also shown. The solution is computed using the AMP-RB scheme with velocity correction on the grid $\mathcal{G}_{\text{rd}}^{(4)}$ with $\Delta t = .05$ and $\beta_d = 1$. The inner disk, with angular velocity equal to $\alpha_b = 1$ initially, rotates counter-clockwise and slows due to the viscous shear stress from the fluid. Even for these light bodies, the numerical solution shows no signs of instabilities. However, the error in angular acceleration $\dot{\omega}_b$ is seen to possess a few small start-up oscillations near $t = 0$, which are expected for these difficult simulations with small ρ_b .

Results of a grid convergence study are given in Table 2. The max-norm errors at $t = 1$ are computed by comparing numerical solutions to the exact solution for the cases of $\rho_b = 10, 1$ and zero, all using $\alpha_b = 0.1$. Convergence rates are also given in the tables and these are estimated using a least-squares fit to the log of the errors. The AMP-RB scheme with velocity correction and $\beta_d = 1$ is used for all of the results. The errors are seen to converge at rates close to second-order accuracy for all cases, including the case of a zero-mass rigid body where added-damping effects are strongest.

8.3. Zero mass disk in a counter-flow

Consider a buoyant and very light rigid disk that is allowed to move within a rectangular fluid domain as shown in Figure 7. The flow in the channel and the motion of the solid disk are initiated from rest by smoothly turning on a pressure gradient (by imposing a time-dependent pressure at inflow and fixing the pressure at outflow) and smoothly turning on a gravitational body force.

The geometry of the problem is shown in Figure 7. The fluid channel covers the rectangular domain $[-x_c, x_c] \times [y_0, y_1]$, where $x_c = 1$, $y_0 = -3$ and $y_1 = 1$. The solid disk, with radius $R_b = 0.2$, is initially

| Rotating disk, $\rho_b = 10$ | | | | | | | | |
|------------------------------|---------|-----|---------|-----|------------------|-----|------------------------|-----|
| $h^{(j)}$ | E_j^p | r | E_j^v | r | $E_j^{\omega_b}$ | r | $E_j^{\dot{\omega}_b}$ | r |
| 1/10 | 6.9e-5 | | 1.2e-4 | | 3.0e-5 | | 2.9e-5 | |
| 1/20 | 1.6e-5 | 4.3 | 3.0e-5 | 4.1 | 8.5e-6 | 3.6 | 7.9e-6 | 3.6 |
| 1/40 | 4.0e-6 | 4.0 | 7.4e-6 | 4.0 | 2.8e-6 | 3.0 | 2.6e-6 | 3.1 |
| 1/80 | 8.9e-7 | 4.5 | 1.9e-6 | 4.0 | 7.8e-7 | 3.6 | 7.1e-7 | 3.7 |
| rate | 2.08 | | 2.01 | | 1.74 | | 1.76 | |

| Rotating disk, $\rho_b = 1$ | | | | | | | | |
|-----------------------------|---------|-----|---------|-----|------------------|-----|------------------------|-----|
| $h^{(j)}$ | E_j^p | r | E_j^v | r | $E_j^{\omega_b}$ | r | $E_j^{\dot{\omega}_b}$ | r |
| 1/10 | 1.2e-5 | | 4.8e-5 | | 5.1e-6 | | 1.8e-5 | |
| 1/20 | 2.5e-6 | 4.7 | 9.5e-6 | 5.1 | 2.6e-6 | 1.9 | 5.0e-6 | 3.5 |
| 1/40 | 5.9e-7 | 4.2 | 2.5e-6 | 3.8 | 6.2e-7 | 4.2 | 1.3e-6 | 3.8 |
| 1/80 | 1.6e-7 | 3.6 | 6.2e-7 | 4.0 | 1.7e-7 | 3.6 | 3.4e-7 | 3.8 |
| rate | 2.06 | | 2.08 | | 1.67 | | 1.89 | |

| Rotating disk, $\rho_b = 0$ | | | | | | | | |
|-----------------------------|---------|-----|---------|-----|------------------|-----|------------------------|-----|
| $h^{(j)}$ | E_j^p | r | E_j^v | r | $E_j^{\omega_b}$ | r | $E_j^{\dot{\omega}_b}$ | r |
| 1/10 | 3.0e-5 | | 1.0e-4 | | 5.5e-5 | | 4.5e-5 | |
| 1/20 | 6.2e-6 | 4.8 | 2.5e-5 | 4.1 | 1.7e-5 | 3.3 | 1.1e-5 | 4.1 |
| 1/40 | 1.5e-6 | 4.1 | 6.4e-6 | 3.9 | 5.0e-6 | 3.4 | 2.9e-6 | 3.8 |
| 1/80 | 3.4e-7 | 4.4 | 1.6e-6 | 3.9 | 1.4e-6 | 3.7 | 7.4e-7 | 3.9 |
| rate | 2.13 | | 2.00 | | 1.78 | | 1.97 | |

Table 2: Rotating disk. Maximum errors and estimated convergence rates at $t = 1$ computed using the AMP-RB scheme with velocity correction for a heavy ($\rho_b = 10$), medium ($\rho_b = 1$) and zero mass ($\rho_b = 0$) rotating disk.

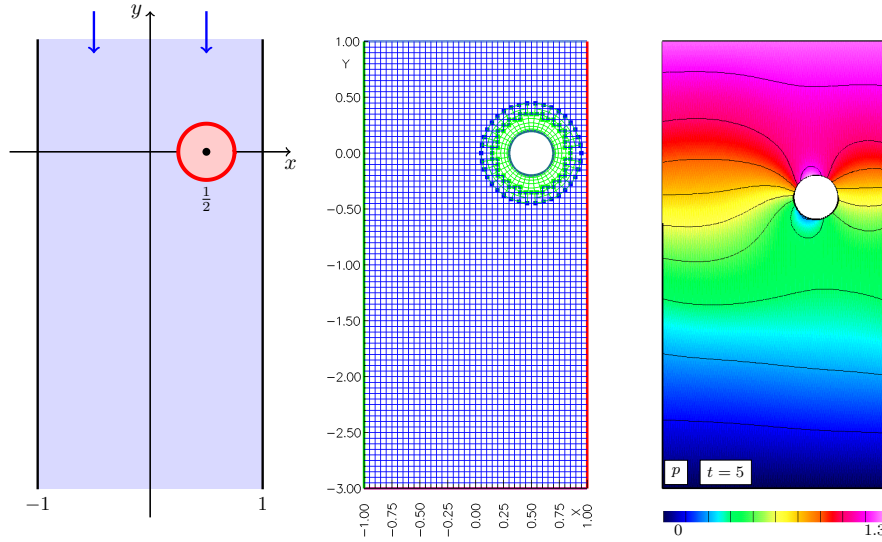


Figure 7: Rising disk in a counter-flow. Left: geometrical configuration at $t = 0$. Middle: Composite grid $\mathcal{G}_{rd}^{(2)}$ at $t = 0$ (coarse grid). Right: contours of the pressure at $t = 5$ using grid $\mathcal{G}_{rd}^{(8)}$.

centred at $(x, y) = (0.5, 0)$. The fluid density and viscosity are taken to be $\rho = 1$ and $\mu = 1$, respectively, and the density of the solid disk is zero, $\rho_b = 0$. At the top boundary of the channel the pressure is specified, the tangential component of the velocity is set to zero, and the normal component of the velocity is extrapolated on the ghost points. The specified pressure at the top ramps smoothly from zero to a value $P_{top} = 1.25$ according to

$$p(x, y_1, t) = P_{top} \mathcal{R}(t),$$

where $\mathcal{R}(t)$ is a *ramp* function given by

$$\mathcal{R}(t) = \begin{cases} (35 + (-84 + (70 - 20t)t)t)t^4, & \text{for } 0 \leq t \leq 1, \\ 1, & \text{for } t > 1. \end{cases} \quad (69)$$

The ramp function satisfies $\mathcal{R} = \mathcal{R}' = \mathcal{R}'' = \mathcal{R}''' = 0$ at $t = 0$ and has three continuous derivatives at $t = 1$. No-slip boundary conditions are taken on the left and right sides of the channel, and on the surface of the solid disk. An outflow boundary condition is taken at the bottom boundary of the channel: the pressure and the normal derivative of the normal component of velocity are both set to zero, and the tangential component of the velocity is extrapolated to the ghost points. The body force due to gravity is smoothly turned on according to

$$\mathbf{f}_e(t) = \pi R_b^2 (\rho_b - \rho) \mathbf{g} \mathcal{R}(t),$$

where the acceleration due to gravity is taken to be $\mathbf{g} = [0, -4]^T$ for the present simulation.

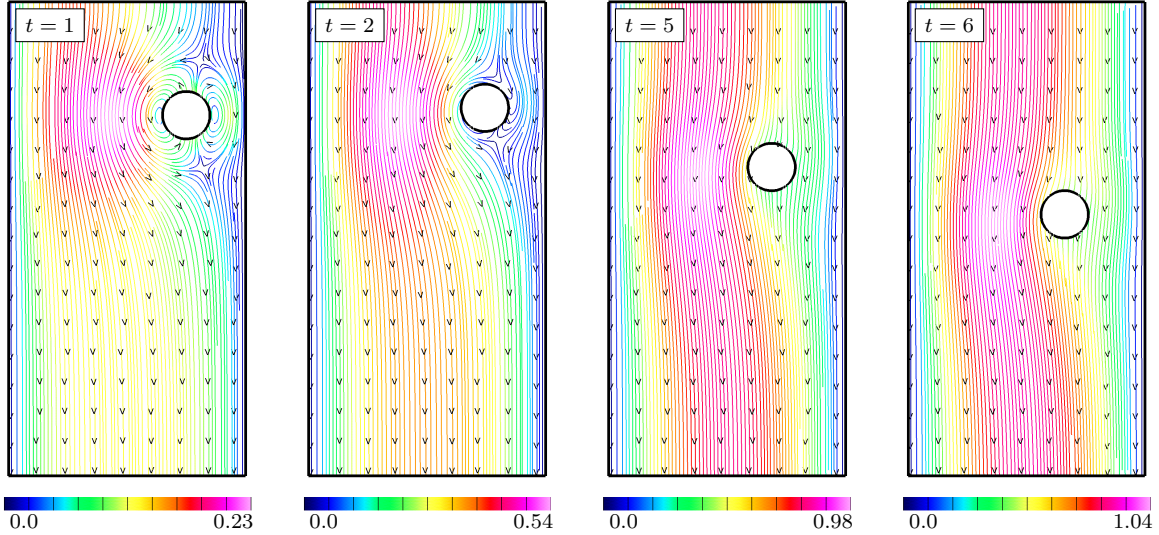


Figure 8: Disk in a counter-flow. Computed streamlines (coloured by the flow speed) at selected times for a moving solid-disk with $\rho_b = 0$, computed using the composite grid $\mathcal{G}_{\text{rd}}^{(8)}$.

The composite grid for the problem at $t = 0$ is shown in Figure 7. The grid with resolution factor j , and target grid spacing $h^{(j)} = 1/(10j)$, is denoted by $\mathcal{G}_{\text{rd}}^{(j)}$, and consists of two component grids. A Cartesian background grid covers the entire domain. An annular grid of fixed radial width equal to 0.2 surrounds the disk. The grid spacing is stretched in the radial direction to be approximately $h_{BL}^{(j)} = h^{(j)}/3$ near the surface of the disk. The time-step is taken as $\Delta t^{(j)} = 0.2 h^{(j)}$.

| $h^{(j)}$ | $E_j^{(p)}$ | r | $E_j^{(u)}$ | r | $E_j^{(v)}$ | r | Max-norm Rate | | | |
|-----------|-------------|-----|-------------|-----|-------------|-----|---------------|------|------|------|
| 1/20 | 6.1e-3 | | 6.4e-4 | | 1.9e-3 | | t | p | u | v |
| 1/40 | 1.3e-3 | 4.6 | 1.3e-4 | 4.8 | 4.1e-4 | 4.7 | 0.5 | 2.19 | 2.27 | 2.22 |
| 1/80 | 2.9e-4 | 4.6 | 2.8e-5 | 4.8 | 8.7e-5 | 4.7 | 1.0 | 2.40 | 2.26 | 2.40 |
| 1/160 | 6.4e-5 | 4.6 | 5.7e-6 | 4.8 | 1.9e-5 | 4.7 | 2.0 | 2.61 | 2.42 | 2.57 |
| rate | 2.19 | | 2.27 | | 2.22 | | 3.0 | 3.26 | 3.20 | 3.00 |

Table 3: Estimated max-norm errors and convergence rates from a self-convergence grid refinement study. Left: results for $t = 0.5$. Right: estimated convergence rates at different times.

Figure 8 shows (instantaneous) streamlines of the solution at a sequence of times. This figure is complemented by the plots in Figure 9 which show the position, velocity and acceleration of the body over time. Initially the disk starts to rise due buoyancy effects but then as the inflow pressure increases the stronger downward flow drives the disk into a downward motion. The centre of the disk moves slowly to the left.

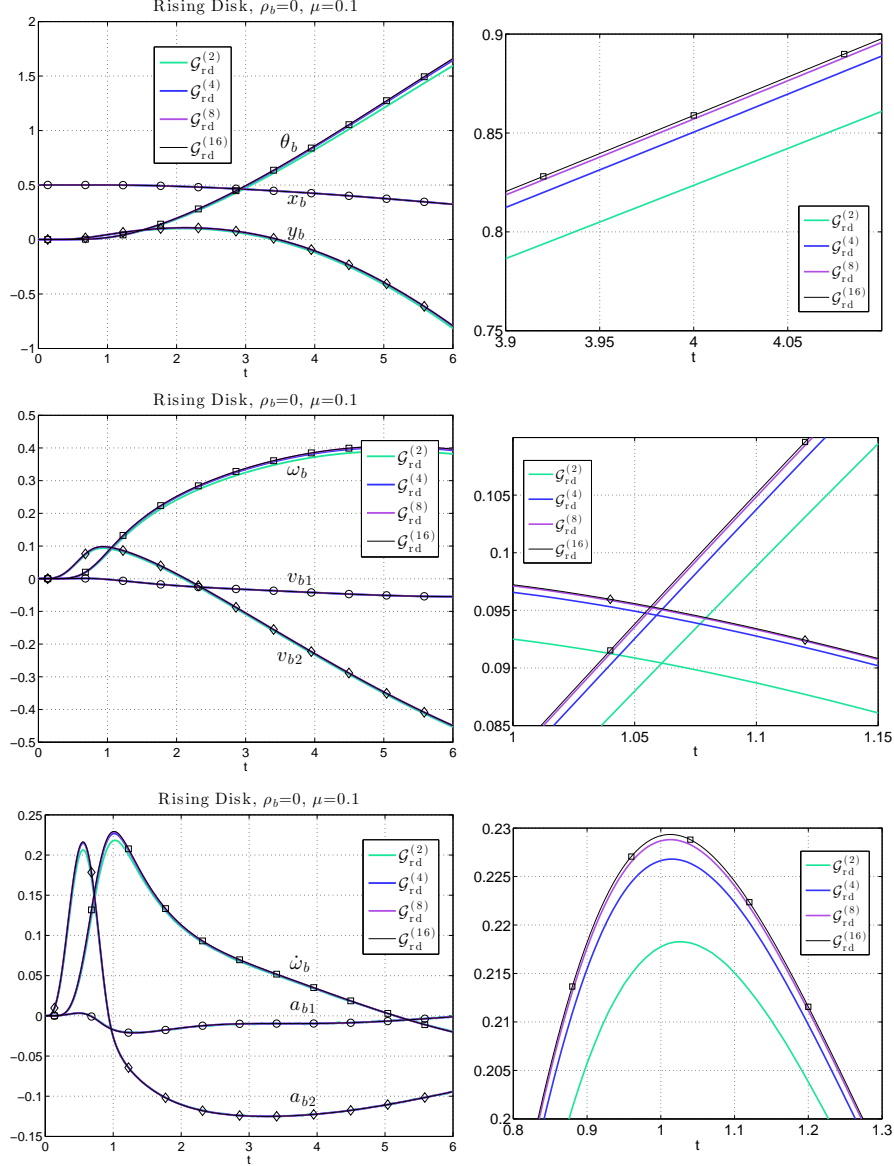


Figure 9: Rising disk in a counter-flow. Time history of the position and angular displacement of a light rigid body (top), its translational and angular velocities (middle), and its accelerations (bottom). The plots on the right show selected enlarged views of the corresponding plots on the left.

| | x_b | y_b | θ_b | v_{b1} | v_{b2} | ω_b | a_{b1} | a_{b2} | $\dot{\omega}_b$ |
|------|-------|-------|------------|----------|----------|------------|----------|----------|------------------|
| rate | 3.17 | 3.17 | 2.02 | 1.96 | 3.34 | 1.98 | 2.61 | 2.52 | 1.95 |

Table 4: Rigid-body time-averaged convergence rates from a self-convergence grid refinement study. These results correspond to the curves in Figure 9.

Table 3 presents estimated convergence rates from a self-convergence grid-refinement study. The rates are computed using a Richardson extrapolation of the results from the finest three grids (see [14] for more details on this procedure). The estimated errors and convergence rates are given at $t = 0.5$ and demonstrate close to second-order accurate convergence. The max-norm rates at different times are also provided and show convergence rates that increase somewhat for later times; this is likely an artifact of the coarse grid solutions not being sufficiently resolved at later times and thus the asymptotic assumptions made in the

Richardson process are not entirely accurate.

Figure 9 shows the motion of the disk as computed on four grids of increasing resolution. Magnified views show that the curves are converging nicely in a manner consistent with second-order accuracy. Table 4 confirms this observation by providing estimated convergence rates computed from a Richardson extrapolation. The values, which are in basic agreement with the rates in Table 3, represent the average rate over time, $t \in [0, 6]$, computed using

$$\text{time-averaged rate} = \log_2 \left(\frac{\|q_n^{(4)} - q_n^{(2)}\|_1}{\|q_n^{(8)} - q_n^{(4)}\|_1} \right),$$

where $\|q_n^{(j)}\|$ denotes the discrete L_1 -norm of the quantity $q_n^{(j)}$ on grid $\mathcal{G}_{\text{rd}}^{(j)}$, over time-steps denoted by n .

8.4. Solid disk falling to the bottom of a fluid chamber

An independent check of the AMP-RB scheme can be made by comparing to solutions obtained by other schemes for a standard test problem available in the literature. One such problem is considered in [15, 16] and involves a moderately heavy solid-disk that falls, due to gravity, in a fluid chamber. The geometry of the problem is shown in the left plot of Figure 10. A solid disk of radius $R_b = 0.5$ is positioned with centre initially at $(0, 0)$ along the centreline and near the top of a rectangular channel with boundaries given by $x_c = 2$, $y_0 = -14$ and $y_1 = 2$. The densities of the fluid and disk are taken to be $\rho = 1$ and $\rho_b = 2$, respectively. In contrast to the zero-mass disk problem studied in Section 8.3, the density of the disk is twice that of the fluid for this test problem, and thus added-mass and added-damping effects are not as strong. No-slip boundary conditions are assumed for the two vertical and bottom horizontal walls of the channel. At the top of the channel, the pressure and the horizontal component of the fluid velocity are set to zero (while the vertical component of the velocity is extrapolated to the ghost point). The fluid and the solid disk are at rest initially, and a downward motion of the disk is initiated by an instantaneous application of a body force given by

$$\mathbf{f}_e(t) = \pi R_b^2 (\rho_b - \rho) \mathbf{g} H(t),$$

where $\mathbf{g} = [0, -g]$ is the acceleration due to gravity and $H(t)$ is the Heaviside function.

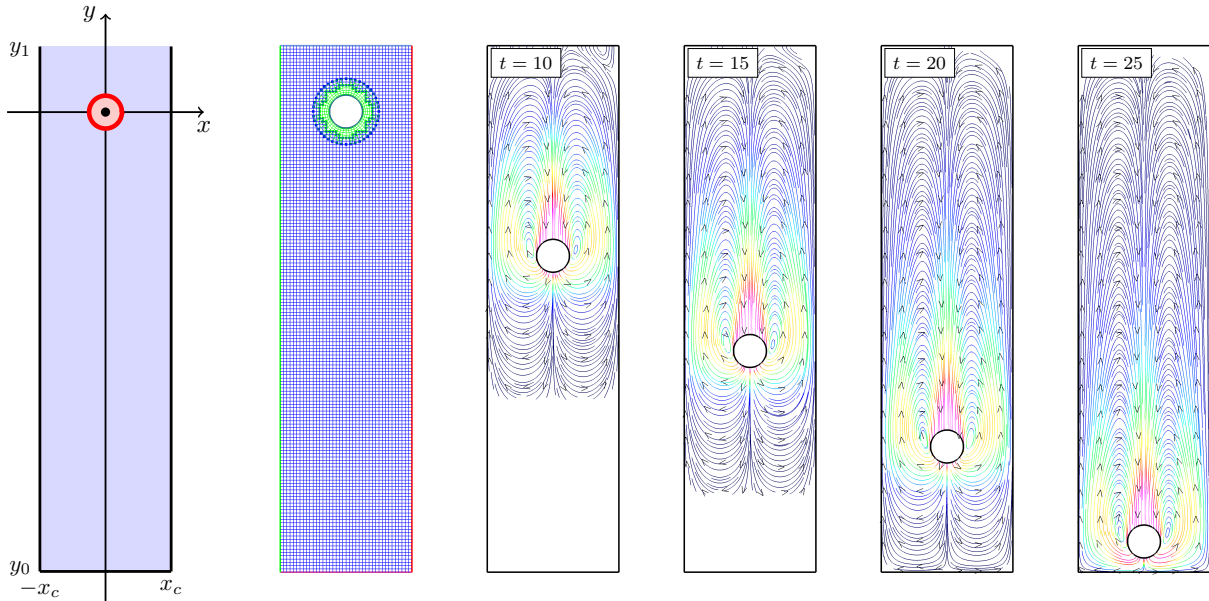


Figure 10: Falling disk in a fluid chamber. Left: Geometrical configuration at $t = 0$. Middle: Composite grid $\mathcal{G}_{\text{fd}}^{(1)}$ at $t = 0$ (coarse grid). Right: Computed streamlines at selected times using grid $\mathcal{G}_{\text{fd}}^{(4)}$.

The results in [15, 16] are described in terms of dimensional quantities, whereas we have chosen to work with dimensionless variables as was done for the previous test problems in this section. The results here can

be converted to dimensional quantities using a reference scale for length given by the diameter of the disk, $\tilde{d} = 0.01$ m, and a reference scale for density given by the fluid density, $\tilde{\rho} = 10^3$ kg/m³. A reference scale for velocity is taken to be an estimate for the terminal velocity of a disk falling in a channel, assuming Stokes flow, given by $\tilde{v}_{\text{term}} = 0.35011$ m/s for the case of a fluid with viscosity given by $\tilde{\mu} = 0.1$ kg/(m s), see [15, 16]. The reference time is thus given by $\tilde{d}/\tilde{v}_{\text{term}} = 0.028562$ s. With these reference scales, the dimensionless fluid viscosity is $\mu = \tilde{\mu}/(\tilde{\rho}\tilde{d}\tilde{v}_{\text{term}}) = 0.028562$, which is the reciprocal of the Reynolds number (based on the diameter of the solid disk), and the dimensionless gravitational constant is $g = \tilde{g}\tilde{d}/(\tilde{v}_{\text{term}})^2 = 0.79949$, where $\tilde{g} = 9.8$ m/s².

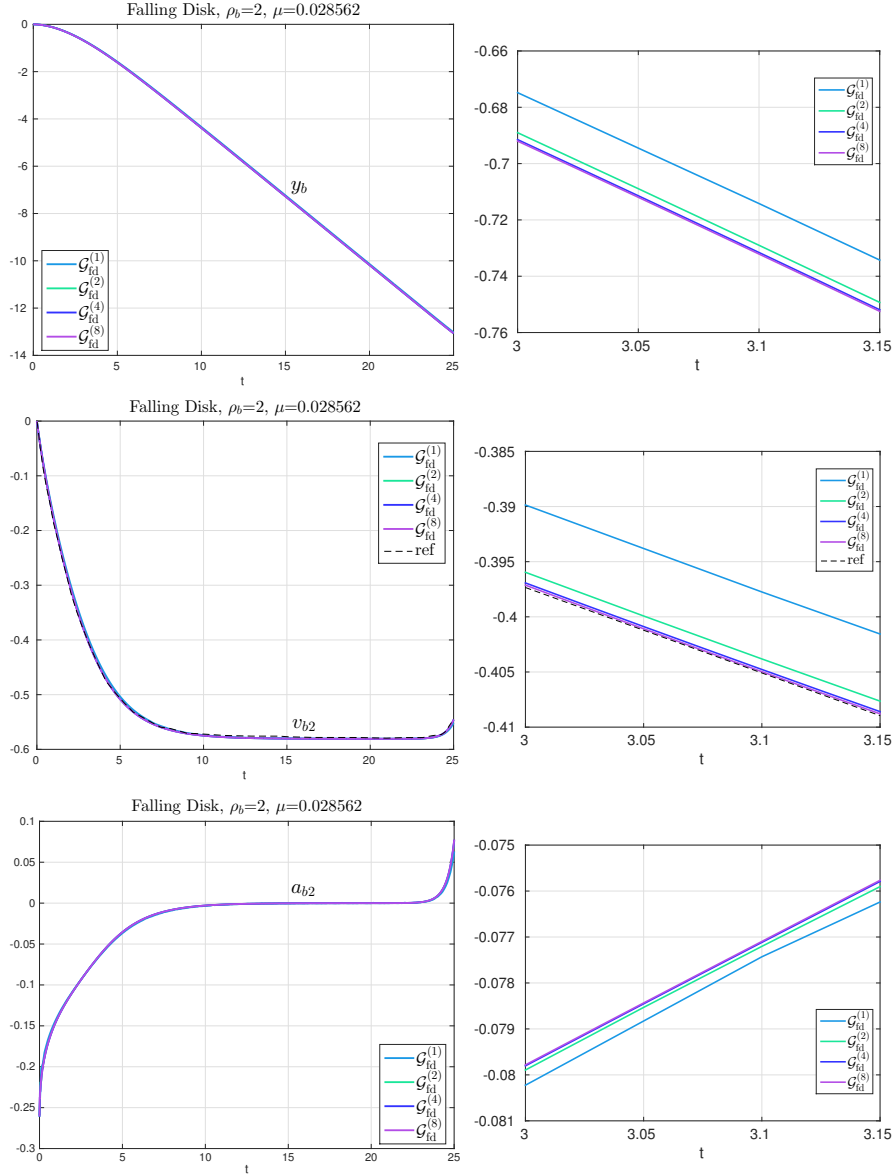


Figure 11: Falling disk in a fluid chamber. Time history of the position (top), velocity (middle) and acceleration (bottom) of the disk in the vertical direction. The plots on the right show selected enlarged views of the corresponding plots on the left. The black dashed-line (“ref”) is taken from Fig. 7.2(b) in [16].

Numerical solutions are computed using the AMP-RB scheme with composite grids of varying resolution, one such grid is shown in Figure 10 for the setup at $t = 0$. The fluid domain in the channel is represented by a background Cartesian grid (shown in blue) and a moving annular body-fitted grid (shown in green). The composite grid has a target grid spacing of $h^{(j)} = 1/(10j)$, with grid resolution factor j , and is denoted

by $\mathcal{G}_{\text{fd}}^{(j)}$. The annular grid has a fixed radial width equal to 0.4 for all grid resolutions. The time-step is taken as $\Delta t^{(j)} = h^{(j)}$.

The streamlines of the solutions at a sequence of times are presented in Figure 10, complemented by Figure 11 which shows the vertical components of the position, y_b , velocity, v_{b2} , and acceleration, a_{b2} , of the falling disk as a function of time, t . The solutions are computed using the composite grid, $\mathcal{G}_{\text{fd}}^{(j)}$, with resolution factors $j = 1, 2, 4$ and 8. The plots in the left column of Figure 11 show the general behaviour of y_b , v_{b2} and a_{b2} , while the plots in the right column show enlarged views which indicate the convergence of the various solution components. The dashed curves in the velocity plots are taken from the numerical results given in Fig. 7.2(b) from [16] for their finest grid resolution which corresponds to our grid $\mathcal{G}_{\text{fd}}^{(4)}$ approximately. We observe that the results computed using the AMP-RB scheme are in excellent agreement with the result from [16], and show a convergence consistent with second-order accuracy. In fact, Richardson-extrapolation estimates for the time-averaged convergence rate are computed as in Section 8.3, and these rates are found to be 2.11 for the position, 2.16 for the velocity and 2.43 for the acceleration, respectively, in agreement with second-order accuracy. The remaining cases in [15, 16] using other choices of the viscosity have been computed using the AMP-RB scheme, and we have found similar agreement and convergence behaviour. Finally, we note that the TP-RB scheme is also stable without sub-iterations for this problem, and produces results nearly identical to the AMP-RB scheme.

8.5. Rectangular body rising to the top of fluid chamber

Consider a light and rectangular-shaped body which rises under buoyancy forces in a heavier fluid and settles near the top of a closed fluid chamber as shown in Figure 12. The fluid with density $\rho = 1$ and viscosity $\mu = 0.025$ occupies the square domain $\Omega = [-1, 1] \times [-1, 1]$ and is at rest initially. No-slip boundary conditions are taken along the four walls of the fluid chamber. The rigid-body is a rectangular solid of width $W_b = 1$, height $H_b = 0.5$ and uniform density $\rho_b = 0.001$, with initial centre-of-mass located at the origin. The corners of the solid are rounded in order to avoid singular behaviour in the solution that can occur near sharp convex corners. The buoyant solid rises under the influence of gravity according to the body force in (5) given by

$$\mathbf{f}_e(t) = A_b(\rho_b - \rho) \mathbf{g} \mathcal{R}(t), \quad (70)$$

where $A_b \approx 0.5$ is the computed area of the solid, $\mathbf{g} = [0, -1]^T$ is an acceleration due to gravity, and the ramp function \mathcal{R} is given by (69).

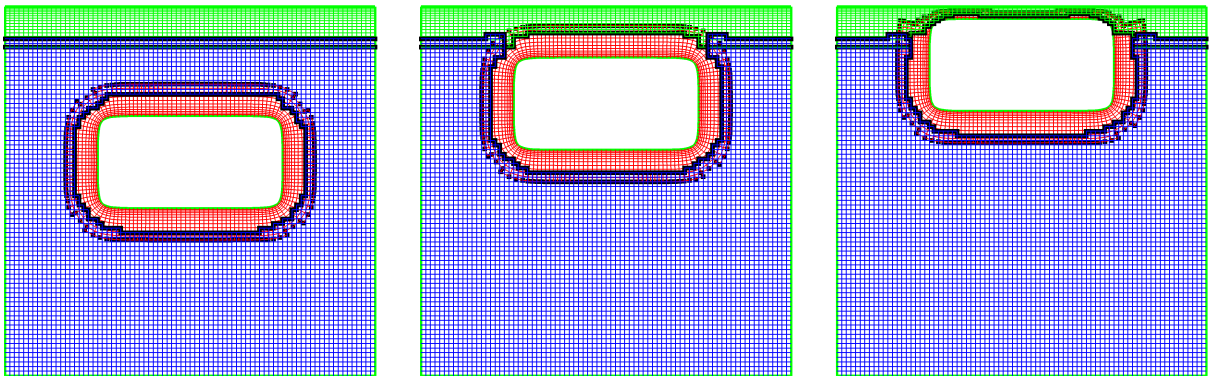


Figure 12: Rising body: Coarse composite grid, $\mathcal{G}_{\text{rb}}^{(4)}$, at times $t = 2, 4$ and 10. The composite grid consists of a background Cartesian component grid, a boundary-fitted grid attached to the surface of the rising solid, and a stretched boundary-fitted grid along the top wall of the fluid chamber with a finer grid resolution to accommodate a close encounter with the rising solid.

The composite grid used for this problem, $\mathcal{G}_{\text{rb}}^{(j)}$, is shown in Figure 12, and consists of a background Cartesian grid (blue), a boundary-fitted grid attached to the surface of the rising solid (red), and a stretched boundary-fitted grid (green) along the top wall of the fluid chamber to accommodate a close encounter with the rising solid. As before, the grid with resolution factor is indicated by the superscript j . The

target background grid spacing is $h^{(j)} = 1/(10j)$, while the target boundary-layer spacing is four times finer, $h_{BL}^{(j)} = h^{(j)}/4$, near the top wall.

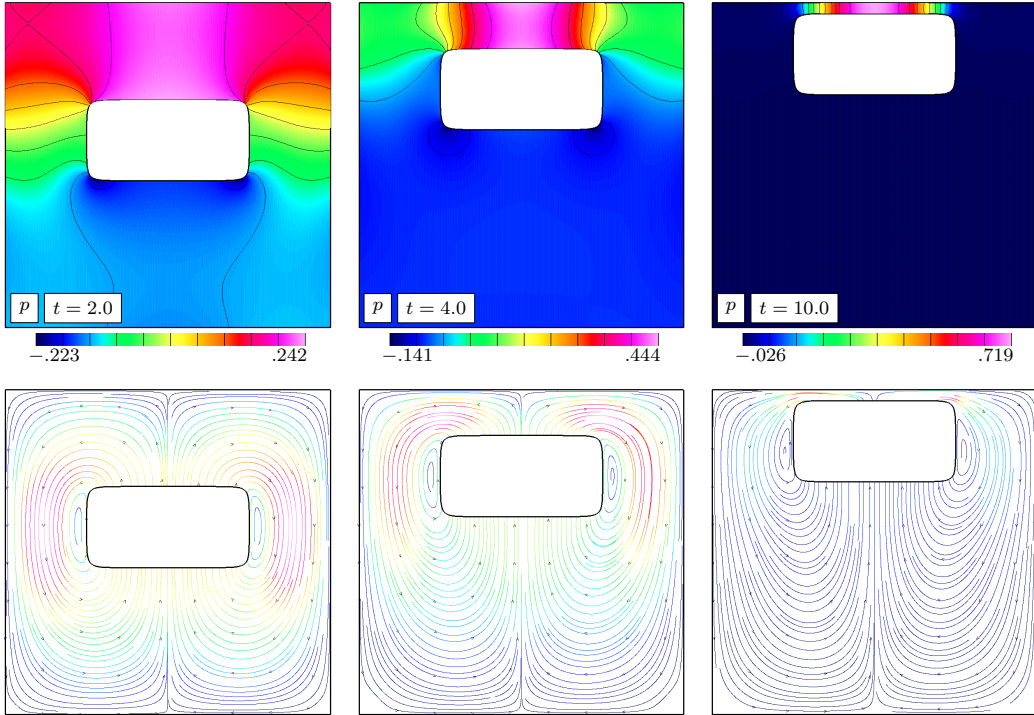


Figure 13: Rising body: Contours of the pressure (top row) and instantaneous streamlines (bottom row) for $\rho_b = 0.001$ at times $t = 2, 4$ and 10 computed using the composite grid $\mathcal{G}_{rb}^{(16)}$.

Figure 13 shows contours of the pressure and (instantaneous) streamlines from the computed solution using the composite grid $\mathcal{G}_{rb}^{(16)}$ for three different times as the solid rises. The time history of the vertical position, $y_b(t)$, and vertical velocity, $v_b(t)$, Figure 14. The rectangular block initially accelerates upwards due to buoyant forces before slowing down as it approaches the top wall. At later times, the solid continues to approach the wall slowly as fluid is expelled from the gap. By $t = 10$ the behaviour of the fluid in the gap between the solid and the top wall is similar to that of classical lubrication theory with the pressure showing negligible variation in the vertical direction.

The behaviours of $y_b(t)$ and $v_b(t)$ are presented from simulations on grids, $\mathcal{G}_{rb}^{(j)}$, of increasing resolution, $j = 4, 8, 16$ and 32 . The self-convergence rates for this problem are not as clean as for the previous cases we have considered for a variety of reasons. One reason is that the time-step changes discontinuously at certain times which likely causes a local first-order error since the added-damping coefficients depend on Δt . Another reason is that the boundary-fitted grids we have constructed become narrower as the grid is refined, to allow a closer approach between the body and wall, but this usually leads to poor estimates for the convergence rates since the region covered by a given grid changes as the grid is refined. However despite these issues, and the difficulty of the problem, the curves for different grid resolutions appear to be converging reasonably well. To give a quantitative sense of the convergence rate, a Richardson extrapolation estimate for the time-averaged convergence rate is computed (as in Section 8.3) using the finest three simulations for the rigid body position and velocity as a function of time. At the early time, $t = 1$, the rates for the position and velocity are estimated as 1.7 and 1.8, respectively, while for a later time, $t = 5$, the corresponding rates are 1.5 and 2.1 respectively.

Figure 15 shows the behaviour of the vertical acceleration of the rigid-body versus time for different grid resolutions. The acceleration of the body is not as smooth as the vertical position or velocity, but this is not unexpected. A closer look at the results for the coarsest grid shows small blips in the acceleration. These blips correspond to small perturbations that are traced to changes in the overlapping grid connectivity as the body-fitted component grid attached to the solid moves. The motion creates changes in the overlap as new

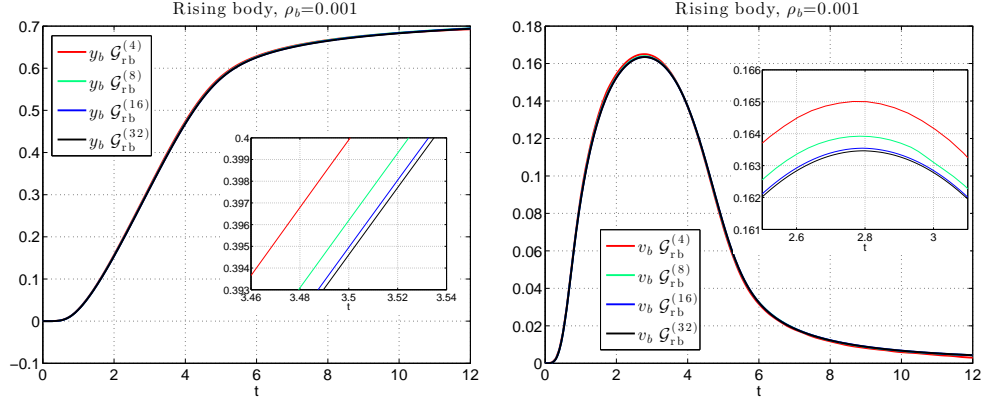


Figure 14: Light rising body: Vertical body position, $y_b(t)$ (left) and vertical velocity of the body, $v_b(t)$ (right), versus time. Results are shown from calculations using the composite grid, $\mathcal{G}_{rb}^{(j)}$, with $j = 4, 8, 16$ and 32 . The zoomed views indicate grid convergence.

interpolation points are computed and as the classification of grid points change between active and inactive (see [4] for a detailed discussion). These changes in the grid result in small perturbations to the pressure and velocity fields, which then are reflected in the fluid forces on the rigid body. The scheme is quite robust to these perturbations which are hardly noticeable in the integrated quantities such as the body velocity and position. In addition, the size of the perturbations is seen to become smaller as the grid is refined. In fact, the time averaged convergence rates using Richardson extrapolation for the acceleration are 1.7 and 1.6 at $t = 1$ and $t = 5$, respectively.

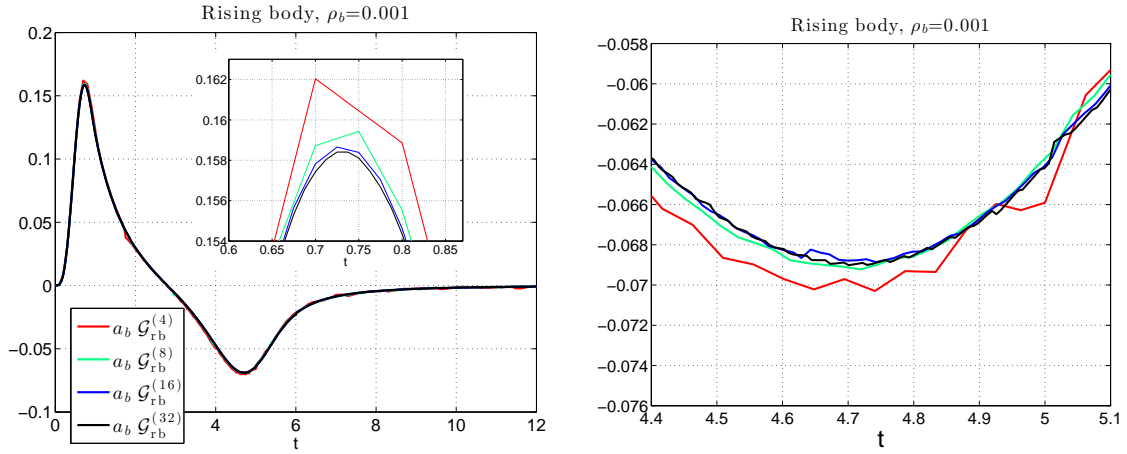


Figure 15: Light rising body. Left: vertical acceleration, $a_b(t)$, of the light rising body. Right: zoom near $t = 4.75$ showing the perturbations to the accelerations caused by the changes in overlapping grid interpolation points as the component grid fitted to the body moves.

It is interesting to discover that instabilities due to added-damping effects can be important for this problem even though the dominant motion is translational. The added-damping terms in the AMP interface condition (34) involve the factor $\beta_d \Delta t$ and the added-damping tensor \mathbf{D} . The components of this tensor are computed from discrete approximations to the surface integrals in (59)–(62) using the discrete geometry defining the rounded rectangular solid. For the grid $\mathcal{G}_{rb}^{(4)}$, for example, the main contributions to \mathbf{D} are found to be

$$\tilde{\mathcal{D}}_{h,11}^{vv} \approx 1.917 \frac{\mu}{\Delta n}, \quad \tilde{\mathcal{D}}_{h,22}^{vv} \approx 0.917 \frac{\mu}{\Delta n}, \quad \tilde{\mathcal{D}}_{h,22}^{\omega\omega} \approx 0.379 \frac{\mu}{\Delta n},$$

with other entries in the added-damping tensor being approximately zero. These contributions are in good agreement with those obtained using the exact surface integrals for a square-cornered rectangular solid which

give

$$\tilde{\mathcal{D}}_{e,11}^{vv} = 2W_b \frac{\mu}{\Delta n} = 2 \frac{\mu}{\Delta n}, \quad \tilde{\mathcal{D}}_{e,22}^{vv} = 2H_b \frac{\mu}{\Delta n} = \frac{\mu}{\Delta n}, \quad \tilde{\mathcal{D}}_{e,22}^{\omega\omega} = \frac{W_b H_b (W_b + H_b)}{2} \frac{\mu}{\Delta n} = \frac{3}{8} \frac{\mu}{\Delta n},$$

(see equation (B.2) in Appendix B). Observe that the added-damping terms are proportional to $\mu\Delta t/\Delta n$, where Δn is defined in (58). For coarser grids where the time-step is larger, $\Delta n \approx \sqrt{\nu\Delta t}/2$ so that the added-damping terms scale as $\sqrt{\nu\Delta t}$. This indicates that added-damping effects increase for larger values of Δt , in agreement with the analysis in Part I. As an example, Figure 16 shows an added-damping instability for a simulation on the grid $\mathcal{G}_{\text{rb}}^{(4)}$ when the added-damping coefficient β_d is intentionally and artificially chosen too small ($\beta_d = 0.5$ in this case). The instability appears primarily as a rotational oscillation of the body while it rises. The time history of the angular acceleration, $\dot{\omega}_b$, shows this high-frequency oscillation. It is interesting to note that the amplitude of this instability saturates due to counter-acting pressure forces caused by added-mass effects.

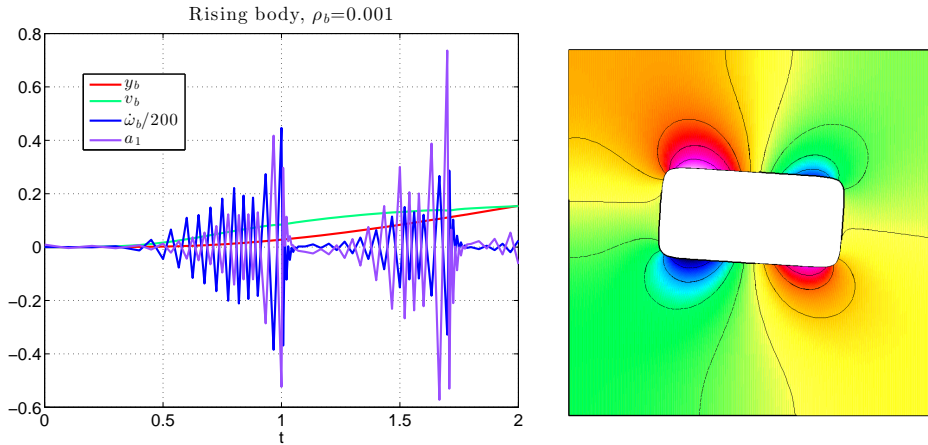


Figure 16: Illustration of the added-damping instability for a light rising-body when the added-damping coefficient β_d is intentionally chosen to be too small. The simulation becomes unstable without sufficient added-damping. The body undergoes unphysical rotations (as reflected in $\dot{\omega}_b$) which are partially stabilized by counter-acting pressure forces (pressure at $t = 1.4$ is shown on right). Results are shown for grid $\mathcal{G}_{\text{rb}}^{(4)}$, with added-damping coefficient $\beta_d = 0.5$.

Finally, note that the results from the traditional scheme for this problem give nearly identical results to those from the AMP-RB scheme. The TP-RB scheme, however, requires many sub-time-step iterations at each time step, 85 on average with a maximum of about 200 at early times, for a simulation using the composite grid $\mathcal{G}_{\text{rb}}^{(4)}$.

8.6. Interaction between rising and falling bodies in a fluid chamber

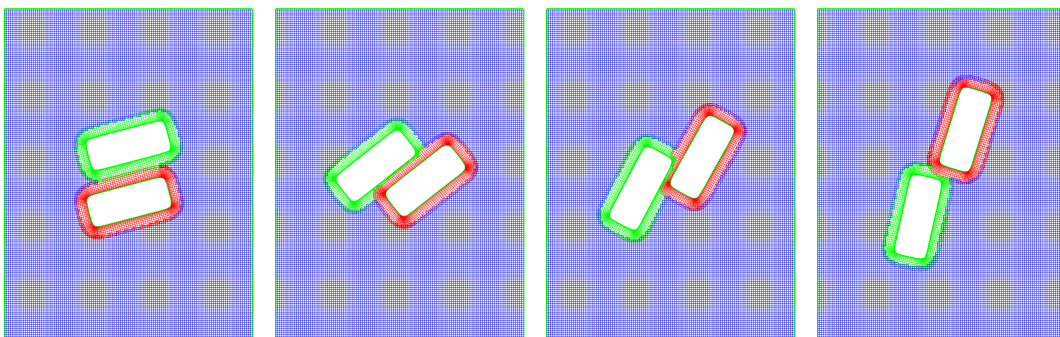


Figure 17: Rising and falling bodies. Composite grid $\mathcal{G}_{\text{rf}}^{(4)}$ at times $t = 1, 8, 10$ and 12 (left to right).

As a final illustration of the AMP-RB scheme, we consider the buoyancy-driven interaction of two rectangular-shaped bodies, initially located one above the other, as shown in Figure 17. The lower and

lighter body (referred henceforth as the *bottom* body) of density $\rho_b = 0.5$ attempts to rise in a fluid of density $\rho = 1$, but is impeded initially by the heavier body above it (referred henceforth as the *top* body) of density $\rho_b = 1.5$ that is attempting to fall. This example demonstrates the properties of the AMP-RB scheme for the case of multiple translating and rotating bodies. The rigid bodies are both considered to be “light” relative the fluid density in that added-mass and added-damping effects are important, and these effects vary over time due to the thin gap between the solids at early times and their relative motion.

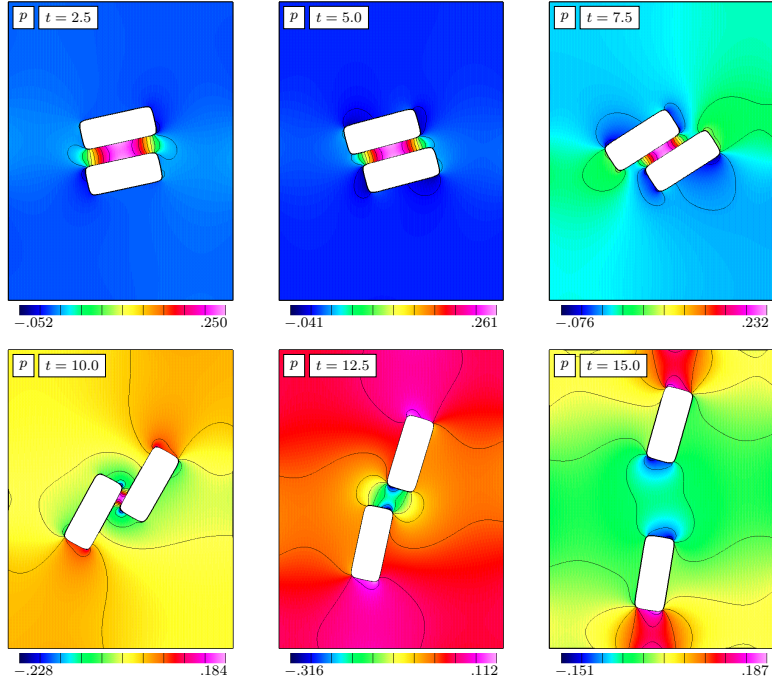


Figure 18: Rising and falling bodies. Contours of the pressure at various times. The results use $\mathcal{G}_{\text{rf}}^{(16)}$.

The fluid domain covers the rectangle $[-1.5, 1.5] \times [-2, 2]$. The solids are rectangles with rounded corners, both of the same shape and with approximate width $W_b = 1$ and height $H_b = 0.4$. The top solid with density $\rho_b = 1.5$ is centred at $(x, y) = (0, 0.35)$ initially and is rotated counter-clockwise by 15° about its centre. The bottom solid with density $\rho_b = 0.5$ is centred at $(x, y) = (0, -0.35)$ initially and is rotated counter-clockwise by 15° about its centre. The composite grid for the domain, denoted by $\mathcal{G}_{\text{rf}}^{(j)}$, where j denotes the resolution factor, consists of three component grids as shown in Figure 17. A Cartesian background grid covers most of the fluid domain, and boundary-fitted grids are attached to the surface of the two bodies. The grid spacing for the Cartesian grid is $\Delta s^{(j)} = 1/(10j)$. The two boundary-fitted grids are stretched in the direction normal to the surface of the bodies so that $\Delta s^{(j)} \approx 1/(10j)$ for the grid lines away from the body, whereas the grids lines near the body surfaces are clustered by a factor of approximately 4.

The boundary conditions for the problem are taken as no-slip walls on the surface of the bodies and all sides of the rectangular fluid domain. The fluid and the solid bodies are at rest initially. The viscosity of the fluid is $\mu = .05$, and a body force given by (70) is taken for each solid with $\mathbf{g} = [0, -1]$. As before, the body force turns on smoothly to avoid an impulsive start.

Shaded contours of the pressure are shown at selected times in Figure 18, while the time-history of the rigid body variables are shown in Figure 19. The latter figure also gives an animation of the translation and rotation of the two bodies over time. The bodies start from rest and the body force due to gravity is turned on smoothly over the time interval $t \in [0, 1]$. The bodies slowly approach one another at early times. During this time, a large pressure develops in the gap between the bodies which reducing the rate at which the gap closes. The top body begins to move to the left while the bottom body moves to the right. At the same time the bodies begin to rotate in a counter-clockwise direction. The bodies continue to slide by each other and rotate. By time $t = 10$ the bodies have nearly separated from one another, and the gap between the bodies becomes quite small (see Figure 18). The angular acceleration of the bodies is the largest in magnitude at about this time. By $t = 12$ the bodies have separated and there is a negative pressure in the remaining gap

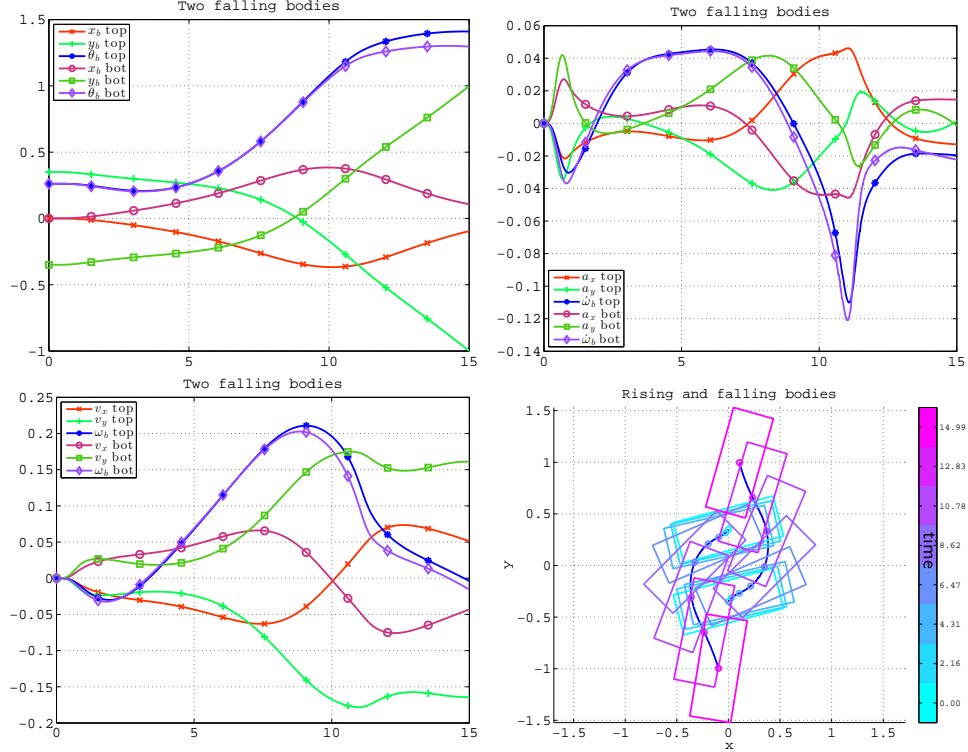


Figure 19: Rising and falling bodies. Time history of the position (top left), velocity (bottom left) and acceleration (top right) of the top and bottom rigid bodies. The bottom-right plot gives a time animation of the locations of the two bodies with the colour indicating time. The results use $\mathcal{G}_{\text{rf}}^{(16)}$.

that keeps the bodies from separating too quickly. The bodies continue to separate and by $t = 15$ they are approaching the lower and upper walls of the fluid container.

Figure 20 shows a grid convergence study for selected rigid body variables; other variables show similar behaviour. As the grid is refined the curves are seen to converge with the separation between curves decreasing rapidly as the grids are refined. The positions and velocities of the bodies are reasonably represented even on the coarsest grid $\mathcal{G}_{\text{rf}}^{(2)}$, although the accelerations on this grid show small oscillations. The amplitude of these oscillations in the acceleration decrease as the grid is refined as we have noted in previous example calculations.

9. Conclusions

In this second part of a two-part series we have developed the general formulation of the AMP-RB scheme for the partitioned solution of rigid bodies moving in an incompressible fluid. This scheme remains stable, without sub-iterations, for light and even zero-mass bodies. The primary extension to multiple space dimensions involved the development of the added-damping tensors; these are incorporated into the equations of motion of the rigid body to address added-damping instabilities. Linearization of the force and torque terms on the rigid-body led to analytic forms for these added-damping tensors whose entries depend on solutions to two vector Helmholtz equations. Approximate forms of these tensors, convenient for use in numerical solutions were developed. The entries in the approximate added-damping tensors, which involving surface integrals over the body, can be pre-computed during a preprocessing step. The AMP-RB scheme was implemented in two dimensions for general domains with one or more rigid bodies by using composite overlapping grids. This is an efficient approach for treating moving body problems and provides smooth boundary fitted grids on the body for accurate treatment of boundary layers.

Numerical results were used to demonstrate the stability and second-order accuracy of the scheme. Some challenging problems involving very light bodies demonstrated the effectiveness of the scheme. The AMP-RB

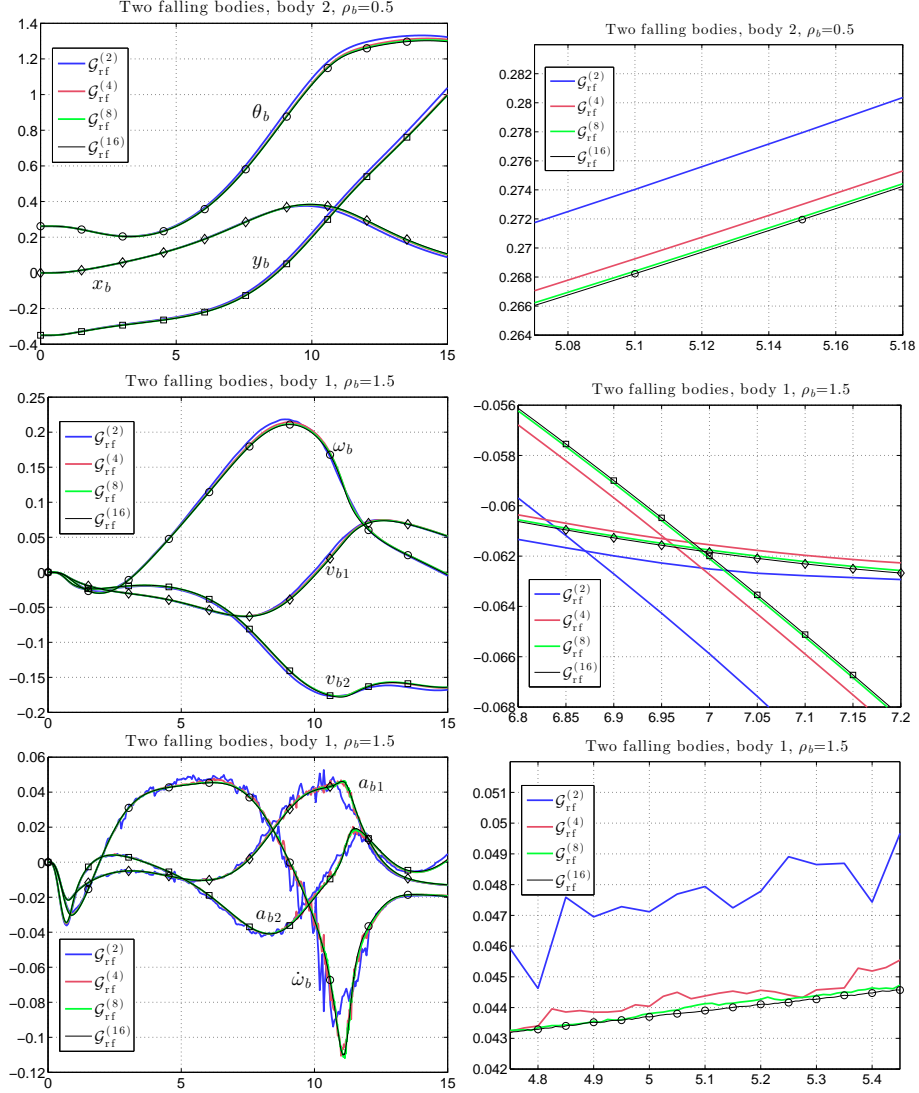


Figure 20: Rising and falling bodies. Grid convergence of representative variables for the rigid bodies. Top: positions x_b , y_b and rotation angle θ_b for body 2. Middle: velocities v_{b1} , v_{b2} and angular velocity ω_b for body 1. Bottom: accelerations a_{b1} , a_{b2} and angular acceleration $\dot{\omega}_b$ for body 1. Corresponding enlarged views are shown on the right.

scheme was shown to produce nearly identical results to the traditional scheme with sub-iterations, although for hard cases the traditional scheme required tens or hundreds of sub-iterations per time-step. Added-damping effects arising from viscous shear stresses are clearly important for rotationally symmetric bodies such as a disk in two dimensions or a sphere in three dimensions. The case of a rising buoyant rectangular body, however, demonstrated that it is also important to account for added-damping effects for body shapes that are far from rotationally symmetric.

In future work we plan to extend the AMP-RB algorithm to three dimensions, which in principal should not present any significant issues. In practice, there are various details that need to be treated properly such as the accurate evaluation of surface integrals on bodies covered by multiple overset grids as needed for computing forces, torques and entries in the added-damping tensors. We will also consider extending the AMP-RB scheme to higher-order accuracy in space and time. For this extension, we note that the spatial discretization of the Navier-Stokes equations to fourth-order accuracy on overset grids has been developed previously in [1], and this could be used as a basis for a fourth-order accurate scheme. Higher-order accurate schemes in time, however, will need to be developed and these will need to be stable within the fractional-step framework. The approximate added-damping tensors developed in this article could be used in the

high-order accurate scheme, likely without change, provided high-order accurate values for the predicted body accelerations are used, but again the stability of such a procedure would need to be evaluated.

Appendix A. Shear stress of an incompressible fluid on the surface of a rigid body

In this section we prove Theorem 1 from Section 3. Let $\mathbf{x} = \mathbf{g}(\mathbf{r}, t)$ be an orthogonal coordinate transformation for the fluid region adjacent to some portion of the body whose surface located at $r_1 = 0$. Thus points $\mathbf{x} \in \Gamma_b$ are of the form $\mathbf{x} = \mathbf{g}(0, r_2, r_3, t)$, where r_2 and r_3 parameterize a portion of the surface. The unit normal $\mathbf{n} = [n_1, n_2, n_3]^T$ to the surface can be written as

$$\mathbf{n} = \frac{1}{\alpha_1} \nabla_{\mathbf{x}} r_1, \quad n_i = \frac{1}{\alpha_1} \frac{\partial r_1}{\partial x_i}, \quad \alpha_1 = \|\nabla_{\mathbf{x}} r_1\|. \quad (\text{A.1})$$

The unit tangent vectors can be written in the form,

$$\mathbf{t}_m = \frac{1}{\alpha_{m+1}} \nabla_{\mathbf{x}} r_{m+1}, \quad \alpha_{m+1} = \|\nabla_{\mathbf{x}} r_{m+1}\|, \quad m = 1, 2. \quad (\text{A.2})$$

The normal and tangent vectors form an orthonormal set. We first derive an expression for the viscous shear stress in terms of the normal and tangential derivatives of the velocity, given by

$$\mathbf{v}_n = \frac{\partial \mathbf{v}}{\partial n} = (\mathbf{n} \cdot \nabla) \mathbf{v} = \alpha_1 \frac{\partial \mathbf{v}}{\partial r_1}, \quad (\text{A.3})$$

$$\mathbf{v}_{t_m} = \frac{\partial \mathbf{v}}{\partial t_m} = (\mathbf{t}_m \cdot \nabla) \mathbf{v} = \alpha_{m+1} \frac{\partial \mathbf{v}}{\partial r_{m+1}}, \quad m = 1, 2, \quad (\text{A.4})$$

which is valid for an incompressible fluid in general unconnected to any rigid body.

Lemma 1. *The viscous shear stress for an incompressible fluid, written in terms of the normal and tangential derivatives of the velocity, is*

$$\boldsymbol{\tau} \mathbf{n} = \mu \sum_{m=1}^2 \left\{ \mathbf{t}_m \mathbf{t}_m^T \frac{\partial \mathbf{v}}{\partial n} + (\mathbf{t}_m \mathbf{n}^T - 2\mathbf{n} \mathbf{t}_m^T) \frac{\partial \mathbf{v}}{\partial t_m} \right\}. \quad (\text{A.5})$$

Proof. The tensor $\nabla \mathbf{v}$ with components $\partial v_i / \partial x_j$ can be written as

$$\nabla \mathbf{v} = \frac{\partial \mathbf{v}}{\partial n} \mathbf{n}^T + \sum_{m=1}^2 \frac{\partial \mathbf{v}}{\partial t_m} \mathbf{t}_m^T. \quad (\text{A.6})$$

Whence the expressions $(\nabla \mathbf{v}) \mathbf{n}$ and $(\nabla \mathbf{v})^T \mathbf{n}$ can be written as

$$(\nabla \mathbf{v}) \mathbf{n} = \mathbf{v}_n = \mathbf{n} \mathbf{n}^T \mathbf{v}_n + \sum_{m=1}^2 \mathbf{t}_m \mathbf{t}_m^T \mathbf{v}_n, \quad (\text{A.7})$$

$$(\nabla \mathbf{v})^T \mathbf{n} = \mathbf{n} \mathbf{n}^T \mathbf{v}_n + \sum_{m=1}^2 \mathbf{t}_m \mathbf{n}^T \mathbf{v}_{t_m}, \quad (\text{A.8})$$

where the final relation in (A.7) comes from the decomposition of the vector \mathbf{v}_n into its normal and tangential components. Using (A.7) and (A.8) gives

$$\frac{1}{\mu} \boldsymbol{\tau} \mathbf{n} = (\nabla \mathbf{v} + (\nabla \mathbf{v})^T) \mathbf{n} = 2\mathbf{n} \mathbf{n}^T \mathbf{v}_n + \sum_{m=1}^2 \mathbf{t}_m \mathbf{t}_m^T \mathbf{v}_n + \mathbf{t}_m \mathbf{n}^T \mathbf{v}_{t_m}. \quad (\text{A.9})$$

Note that $\nabla \cdot \mathbf{v} = 0$ implies

$$\mathbf{n}^T \frac{\partial \mathbf{v}}{\partial n} = - \sum_{m=1}^2 \mathbf{t}_m^T \frac{\partial \mathbf{v}}{\partial t_m}, \quad (\text{A.10})$$

since, using (A.1) for \mathbf{n} and (A.2) for \mathbf{t}_m together with (A.3) and (A.4),

$$\begin{aligned} \mathbf{n}^T \frac{\partial \mathbf{v}}{\partial n} + \sum_{m=1}^2 \mathbf{t}_m^T \frac{\partial \mathbf{v}}{\partial t_m} &= \sum_{j=1}^3 \left\{ \frac{1}{\alpha_1} \frac{\partial r_1}{\partial x_j} \alpha_1 \frac{\partial v_j}{\partial r_1} + \sum_{m=1}^2 \frac{1}{\alpha_{m+1}} \frac{\partial r_{m+1}}{\partial x_j} \alpha_{m+1} \frac{\partial v_j}{\partial r_{m+1}} \right\}, \\ &= \sum_{j=1}^3 \sum_{k=1}^3 \frac{\partial r_k}{\partial x_j} \frac{\partial v_j}{\partial r_k} = \sum_{j=1}^3 \frac{\partial v_j}{\partial x_j} = \nabla \cdot \mathbf{v} = 0. \end{aligned}$$

Using (A.10) in (A.9) gives

$$\frac{1}{\mu} \boldsymbol{\tau} \mathbf{n} = \sum_{m=1}^2 \{ \mathbf{t}_m \mathbf{t}_m^T \mathbf{v}_n + (\mathbf{t}_m \mathbf{n}^T - 2\mathbf{n} \mathbf{t}_m^T) \mathbf{v}_{t_m} \},$$

which proves the lemma. \square

Lemma 2. *The vectors in the orthonormal set $\{\mathbf{n}, \mathbf{t}_1, \mathbf{t}_2\}$ satisfy*

$$\mathbf{n} \mathbf{n}^T + \mathbf{t}_1 \mathbf{t}_1^T + \mathbf{t}_2 \mathbf{t}_2^T = \mathbf{I}, \quad (\text{A.11})$$

$$\mathbf{t}_2 \mathbf{t}_1^T - \mathbf{t}_1 \mathbf{t}_2^T = \pm [\mathbf{n}]_{\times}, \quad (\text{A.12})$$

where the sign of the right-hand-side is positive if the set is right-handed and negative otherwise.

Proof. Equation (A.11) holds for any orthonormal set since $\mathbf{x} = \mathbf{n} \mathbf{n}^T \mathbf{x} + \mathbf{t}_1 \mathbf{t}_1^T \mathbf{x} + \mathbf{t}_2 \mathbf{t}_2^T \mathbf{x}$ for any vector \mathbf{x} . For a right-handed set, equation (A.12), with the plus sign, follows since $\mathbf{n} \times \mathbf{n} = 0$, $\mathbf{n} \times \mathbf{t}_1 = \mathbf{t}_2$ and $\mathbf{n} \times \mathbf{t}_2 = -\mathbf{t}_1$. For a left-handed set the sign is reversed. \square

Condition (A.5) for $\boldsymbol{\tau} \mathbf{n}$ can now be specialized to the surface of a rigid body. By taking tangential derivatives of the interface condition

$$\mathbf{v}(\mathbf{x}, t) = \mathbf{v}_b(t) + \boldsymbol{\omega}_b(t) \times (\mathbf{x} - \mathbf{x}_b(t)), \quad \mathbf{x} \in \Gamma,$$

it follows that the tangential derivatives of \mathbf{v} on the rigid body are given by

$$\frac{\partial \mathbf{v}}{\partial t_m} = \boldsymbol{\omega}_b(t) \times \frac{\partial \mathbf{x}}{\partial t_m} = \boldsymbol{\omega}_b(t) \times \mathbf{t}_m, \quad \mathbf{x} \in \Gamma,$$

using $\partial \mathbf{x} / \partial t_m = \mathbf{t}_m$. Thus

$$\begin{aligned} \frac{1}{\mu} \boldsymbol{\tau} \mathbf{n} &= \sum_{m=1}^2 \{ \mathbf{t}_m \mathbf{t}_m^T \mathbf{v}_n + (\mathbf{t}_m \mathbf{n}^T - 2\mathbf{n} \mathbf{t}_m^T) (\boldsymbol{\omega}_b(t) \times \mathbf{t}_m) \}, \\ &= (\mathbf{I} - \mathbf{n} \mathbf{n}^T) \mathbf{v}_n + \sum_{m=1}^2 \{ \mathbf{t}_m \mathbf{n}^T (\boldsymbol{\omega}_b(t) \times \mathbf{t}_m) \} = (\mathbf{I} - \mathbf{n} \mathbf{n}^T) \mathbf{v}_n + \sum_{m=1}^2 \mathbf{t}_m \{ \boldsymbol{\omega}_b(t)^T (\mathbf{t}_m \times \mathbf{n}) \}, \\ &= (\mathbf{I} - \mathbf{n} \mathbf{n}^T) \mathbf{v}_n \pm (-\mathbf{t}_1 \mathbf{t}_2^T + \mathbf{t}_2 \mathbf{t}_1^T) \boldsymbol{\omega}_b(t) = (\mathbf{I} - \mathbf{n} \mathbf{n}^T) \mathbf{v}_n + [\mathbf{n}]_{\times} \boldsymbol{\omega}_b(t), \end{aligned}$$

where the \pm sign depends on whether the system is right-handed or left-handed and where we have used the fact that \mathbf{t}_m and $\boldsymbol{\omega}_b(t) \times \mathbf{t}_m$ are orthogonal. This completes the proof of Theorem 1.

Appendix B. Example added-damping tensors for bodies of different shapes

In this section, examples of the approximate added-damping tensors (59)–(62) are presented for rigid bodies of different shapes. The entries in the tensors are computed analytically by assuming that $\Delta n = \Delta n_{\mathbf{i}}$ is constant for $\mathbf{i} \in \Gamma_h$, and by replacing the surface quadratures in (59)–(62) by surface integrals. These examples can provide some intuition for relating the geometry of a body to the form and magnitude of the added-damping as the body translates or rotates. Recall that as the bodies rotate the added-damping tensors transform according to (29).

Appendix B.1. Cylinder and disk

For a solid three-dimensional circular cylinder of radius a and depth d aligned with the z -axis the moment of inertia about the centre of the disk is

$$\mathbf{I}_b = \begin{bmatrix} I_x & 0 & 0 \\ 0 & I_y & 0 \\ 0 & 0 & I_z \end{bmatrix}, \quad I_x = I_y = \frac{\bar{m}}{12}(3a^2 + d^2), \quad I_z = \frac{\bar{m}}{2}a^2.$$

For a cylinder restricted to rotate about the z -axis, the approximate added-damping tensors (59)–(62) are (ignoring the top and bottom circular faces so that the result can be restricted to a two-dimensional disk)

$$\tilde{\mathcal{D}}^{vv} = \frac{\mu}{\Delta n} \pi a d \begin{bmatrix} 1 & 0 & 0 \\ 0 & 1 & 0 \\ 0 & 0 & 0 \end{bmatrix}, \quad \tilde{\mathcal{D}}^{v\omega} = \tilde{\mathcal{D}}^{\omega v} = \mathbf{0}, \quad \tilde{\mathcal{D}}^{\omega\omega} = \frac{\mu}{\Delta n} (2\pi a d) a^2 \begin{bmatrix} 0 & 0 & 0 \\ 0 & 0 & 0 \\ 0 & 0 & 1 \end{bmatrix}. \quad (\text{B.1})$$

Notice that the entries $\tilde{\mathcal{D}}_{11}^{vv}$ and $\tilde{\mathcal{D}}_{22}^{vv}$ in $\tilde{\mathcal{D}}^{vv}$ are the product of $\mu/\Delta n$ and one half of the surface area of the disk, $S = 2\pi a d$. These values indicate the contribution to the added damping from motions in the x - and y -directions, respectively. The entry $\tilde{\mathcal{D}}_{22}^{\omega\omega}$ in $\tilde{\mathcal{D}}^{\omega\omega}$ is the product of the disk surface area S and the square of the radius. The surface area S is the area over which a shear force could act and this is multiplied by the radius of the disk squared. The effective moment of inertial for rotations about the z -axis is thus

$$I_z + \Delta t \tilde{\mathcal{D}}_{22}^{\omega\omega} = \frac{\bar{m}}{2} a^2 + \Delta t \frac{\mu}{\Delta n} (2\pi a d) a^2$$

Appendix B.2. Rectangle

Consider a solid rectangle of constant density ρ_b with width w in the x -direction and height h in the y -direction. The moment of inertia about the centre of mass for rotations in the plane about the z -axis is

$$I_z = \frac{\bar{m}}{12}(w^2 + h^2) = \frac{\rho_b w h}{12}(w^2 + h^2).$$

The added-damping tensors (59)–(62) for the rectangle are

$$\tilde{\mathcal{D}}^{vv} = \frac{\mu}{\Delta n} \begin{bmatrix} 2w & 0 & 0 \\ 0 & 2h & 0 \\ 0 & 0 & 0 \end{bmatrix}, \quad \tilde{\mathcal{D}}^{v\omega} = \tilde{\mathcal{D}}^{\omega v} = \mathbf{0}, \quad \tilde{\mathcal{D}}^{\omega\omega} = \frac{\mu}{\Delta n} 2(w+h) \frac{w}{2} \frac{h}{2} \begin{bmatrix} 0 & 0 & 0 \\ 0 & 0 & 0 \\ 0 & 0 & 1 \end{bmatrix}. \quad (\text{B.2})$$

The entries $\tilde{\mathcal{D}}_{11}^{vv}$ and $\tilde{\mathcal{D}}_{22}^{vv}$ in $\tilde{\mathcal{D}}^{vv}$ are the product $\mu/\Delta n$ and the surface areas in the x - and y -directions, respectively. These values indicate the contribution to the added damping from motions in the x - and y -directions, respectively. The entry $\tilde{\mathcal{D}}_{22}^{\omega\omega}$ in $\tilde{\mathcal{D}}^{\omega\omega}$ is the product of the surface area of the rectangle $S = 2(w+h)$ and the quantity $\frac{w}{2} \frac{h}{2}$ which corresponds to the radius-squared term for the the disk in (B.1).

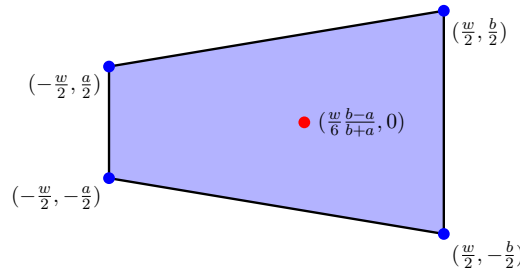


Figure B.21: Geometry of the trapezoid used for computation of the added-damping tensors. The centre of mass is marked as a solid red circle.

Appendix B.3. Trapezoid

Consider a solid trapezoid of constant density ρ_b as shown in Figure B.21. The moment of inertia about the centre of mass for rotations about the z -axis is

$$I_z = \frac{\rho_b w}{12} \frac{(a+b)}{2} \left(w^2 \frac{2}{3} \frac{(a^2 + 4ab + b^2)}{(a+b)^2} + \frac{a^2 + b^2}{2} \right).$$

The approximate added-damping tensors are

$$\tilde{\mathcal{D}}^{vv} = \frac{\mu}{\Delta n} \begin{bmatrix} \frac{4w^2}{\Delta} & 0 & 0 \\ 0 & a+b + \frac{(a-b)^2}{\Delta} & 0 \\ 0 & 0 & 0 \end{bmatrix}, \quad \tilde{\mathcal{D}}^{v\omega} = (\tilde{\mathcal{D}}^{\omega v})^T = \frac{\mu}{\Delta n} \frac{w}{3} (b-a) \left(1 - \frac{2}{\Delta} \frac{a^2 + ab + b^2}{a+b} \right) \begin{bmatrix} 0 & 0 & 0 \\ 0 & 0 & 1 \\ 0 & 0 & 0 \end{bmatrix},$$

$$\tilde{\mathcal{D}}^{\omega\omega} = \frac{\mu}{\Delta n} \frac{w^2}{9} \left(\frac{a^2 + 7ab + b^2}{a+b} + \frac{4}{\Delta} \frac{(a^2 + ab + b^2)^2}{(a+b)^2} \right) \begin{bmatrix} 0 & 0 & 0 \\ 0 & 0 & 0 \\ 0 & 0 & 1 \end{bmatrix},$$

where

$$\Delta = \sqrt{4w^2 + (a-b)^2}.$$

In this example there can be non-zero entries in $\tilde{\mathcal{D}}^{v\omega}$ and $\tilde{\mathcal{D}}^{\omega v}$, which can be interpreted as follows. The entry $\tilde{\mathcal{D}}_{2,3}^{v\omega}$ represents a force in the y -direction, in the equation for \bar{v}_2 , due to unequal shear forces arising from rotation about the centre of mass (e.g. the shear force on the left face under a rotation is different from the shear force on the right face if $a \neq b$). The entry $\tilde{\mathcal{D}}_{3,2}^{\omega v}$ represents a torque about the centre of mass due to motions in the y -direction, again due to the torque that arises from unequal shear forces.

Appendix B.4. L-shaped domain

Consider an L-shaped domain of constant density ρ_b as shown in Figure B.22. The moment of inertia about the centre of mass for rotations about the z -axis is

$$I_z = \frac{11}{12} \rho_b ab(a^2 + b^2).$$

The approximate added-damping tensors are

$$\tilde{\mathcal{D}}^{vv} = \frac{\mu}{\Delta n} \begin{bmatrix} 4b & 0 & 0 \\ 0 & 4a & 0 \\ 0 & 0 & 0 \end{bmatrix}, \quad \tilde{\mathcal{D}}^{v\omega} = (\tilde{\mathcal{D}}^{\omega v})^T = \frac{\mu}{\Delta n} \frac{1}{3} ab \begin{bmatrix} 0 & 0 & 1 \\ 0 & 0 & -1 \\ 0 & 0 & 0 \end{bmatrix}, \quad \tilde{\mathcal{D}}^{\omega\omega} = \frac{\mu}{\Delta n} \frac{25}{9} ab(a+b) \begin{bmatrix} 0 & 0 & 0 \\ 0 & 0 & 0 \\ 0 & 0 & 1 \end{bmatrix}.$$

The non-zero entries in $\tilde{\mathcal{D}}^{v\omega}$ and $\tilde{\mathcal{D}}^{\omega v}$ can be interpreted following a similar explanation as for the trapezoid, i.e. translations of the body can cause rotational added-damping effects, while rotations can cause translational added-damping effects.

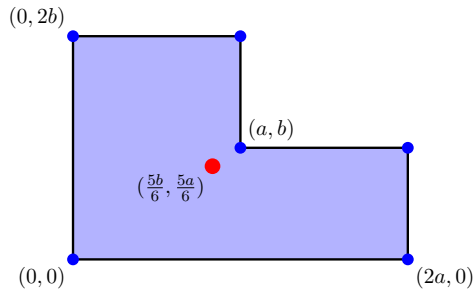


Figure B.22: An L-shaped domain use in the computation of added-damping tensors. The centre of mass is at $(5b/6, 5a/6)$.

Appendix B.5. Ellipse

The approximate added-damping tensors for an ellipse with boundary $(x/a)^2 + (y/b)^2 = 1$, rotating about the z -axis are

$$\begin{aligned} \tilde{\mathcal{D}}^{vv} &= \frac{\mu}{\Delta n} \begin{bmatrix} \mathcal{D}_{11}^{vv} & 0 & 0 \\ 0 & \mathcal{D}_{22}^{vv} & 0 \\ 0 & 0 & 0 \end{bmatrix}, \quad \tilde{\mathcal{D}}^{v\omega} = \tilde{\mathcal{D}}^{\omega v} = \mathbf{0}, \quad \tilde{\mathcal{D}}^{\omega\omega} = \frac{\mu}{\Delta n} \begin{bmatrix} 0 & 0 & 0 \\ 0 & 0 & 0 \\ 0 & 0 & \mathcal{D}_{33}^{\omega\omega} \end{bmatrix}, \\ \tilde{\mathcal{D}}_{11}^{vv} &= -4a \frac{b^2 K(\eta) - a^2 E(\eta)}{a^2 - b^2}, \quad \tilde{\mathcal{D}}_{22}^{vv} = 4b^2 a \frac{K(\eta) - E(\eta)}{a^2 - b^2}, \quad \tilde{\mathcal{D}}_{33}^{\omega\omega} = 4ab^2 K(\eta), \\ \eta &= \frac{(a^2 - b^2)^{1/2}}{a}, \quad K(\eta) = \int_0^1 \frac{1}{\sqrt{(1-t^2)(1-\eta^2 t^2)}} dt, \quad E(\eta) = \int_0^1 \frac{\sqrt{1-\eta^2 t^2}}{\sqrt{1-t^2}} dt \end{aligned}$$

where K is the complete elliptic integral of the first kind and E is the complete elliptic integral of the second kind.

Appendix B.6. Sphere

The approximate added-damping tensors for a sphere of radius a rotating about its centre are

$$\tilde{\mathcal{D}}^{vv} = \frac{\mu}{\Delta n} \frac{8}{3} \pi a^2 \begin{bmatrix} 1 & 0 & 0 \\ 0 & 1 & 0 \\ 0 & 0 & 1 \end{bmatrix}, \quad \tilde{\mathcal{D}}^{v\omega} = \mathbf{0}, \quad \tilde{\mathcal{D}}^{\omega\omega} = \frac{\mu}{\Delta n} \frac{8}{3} \pi a^4 \begin{bmatrix} 1 & 0 & 0 \\ 0 & 1 & 0 \\ 0 & 0 & 1 \end{bmatrix}.$$

References

- [1] W. D. Henshaw, A fourth-order accurate method for the incompressible Navier-Stokes equations on overlapping grids, *J. Comput. Phys.* 113 (1) (1994) 13–25.
- [2] W. D. Henshaw, N. A. Petersson, A split-step scheme for the incompressible Navier-Stokes equations, in: M. M. Hafez (Ed.), *Numerical Simulation of Incompressible Flows*, World Scientific, 2003, pp. 108–125.
- [3] J. W. Banks, W. D. Henshaw, D. W. Schwendeman, Q. Tang, A stable partitioned FSI algorithm for rigid bodies and incompressible flow. Part I: Model problem analysis., preprint arXiv:1611.05711, arXiv, submitted for publication (2016).
- [4] W. D. Henshaw, D. W. Schwendeman, Moving overlapping grids with adaptive mesh refinement for high-speed reactive and non-reactive flow, *J. Comput. Phys.* 216 (2) (2006) 744–779.
- [5] A. Koblitz, S. Lovett, N. Nikiforakis, W. D. Henshaw, Direct numerical simulation of particulate flows with an overset grid method, preprint arXiv:1702.01021, arXiv, submitted for publication (2016).
- [6] F. C. Dougherty, J.-H. Kuan, Transonic store separation using a three-dimensional Chimera grid scheme, paper 89-0637, AIAA (1989).
- [7] Overset Grid Symposium web page, oversetGridSymposium.org.
- [8] D. V. Widder, *Advanced Calculus*, Dover, New York, 1989.
- [9] N. A. Petersson, Stability of pressure boundary conditions for Stokes and Navier-Stokes equations, *J. Comput. Phys.* 172 (1) (2001) 40–70.
- [10] J. W. Banks, W. D. Henshaw, B. Sjögren, A stable FSI algorithm for light rigid bodies in compressible flow, *J. Comput. Phys.* 245 (2013) 399–430.
- [11] J. W. Banks, W. D. Henshaw, D. W. Schwendeman, Deforming composite grids for solving fluid structure problems, *J. Comput. Phys.* 231 (9) (2012) 3518–3547.

- [12] J. W. Banks, W. D. Henshaw, A. Kapila, D. W. Schwendeman, An added-mass partitioned algorithm for fluid-structure interactions of compressible fluids and nonlinear solids, *J. Comput. Phys.* 305 (2016) 1037–1064.
- [13] L. Li, W. D. Henshaw, J. W. Banks, D. W. Schwendeman, G. A. Main, A stable partitioned FSI algorithm for incompressible flow and deforming beams, *J. Comput. Phys.* 312 (2016) 272–306.
- [14] W. D. Henshaw, D. W. Schwendeman, Parallel computation of three-dimensional flows using overlapping grids with adaptive mesh refinement, *J. Comput. Phys.* 227 (16) (2008) 7469–7502.
- [15] A. Robinson-Mosher, C. Schroeder, R. Fedkiw, A symmetric positive definite formulation for monolithic fluid structure interaction, *J. Comput. Phys.* 230 (4) (2011) 1547–1566.
- [16] F. Gibou, C. Min, Efficient symmetric positive definite second-order accurate monolithic solver for fluid/solid interactions, *J. Comput. Phys.* 231 (8) (2012) 3246–3263.